8-2013

Hindered Rotation of Dihydrogen on Synthesized Metal Oxides

George Houston Rouvelas
grouvela@utk.edu

To the Graduate Council:

I am submitting herewith a thesis written by George Houston Rouvelas entitled "Hindered Rotation of Dihydrogen on Synthesized Metal Oxides." I have examined the final electronic copy of this thesis for form and content and recommend that it be accepted in partial fulfillment of the requirements for the degree of Master of Science, with a major in Chemistry.

John Z. Larese, Major Professor

We have read this thesis and recommend its acceptance:

Ziling Xue, Robert J. Hinde

Accepted for the Council:
Carolyn R. Hodges

Vice Provost and Dean of the Graduate School

(Original signatures are on file with official student records.)

Hindered Rotation of Dihydrogen on Synthesized Metal Oxides

A Thesis Presented for the

Master of Science

Degree

The University of Tennessee, Knoxville

George Houston Rouvelas

August 2013

For Mom, Dad, and Sister: I love you more than words adequately express.

Acknowledgements

I would first like to acknowledge my parents, for they have been the most loving, supportive, and patient parents any child could have ever asked for. I realize that there is no way to repay this debt, only to pay it forward to my own children. I would also like to thank my thesis advisor, John Larese. Professor Larese has made an enormously positive impact on not only my scientific career, but my personal growth as a human being and I will sorely miss our daily interaction. Professor Larese has always been more than fair to me, ever since I walked into his office in 2005 as a freshman begging for mercy having just taken his general chemistry final. His physical chemistry lab course transformed not only my scientific writing skills, but everyone else who was serious about his course. When I was intent on giving up, he did not, and as a vote of confidence awarded me the JINS fellowship. To him I am forever indebted as well, and I pledge to pay it forward to others I may be fortunate enough to mentor. All of the figures in this thesis regarding inelastic neutron scattering are not my own. These INS spectra were made possible by many years of careful experiment planning and execution of Professor Larese and many of our colleagues along the way, to all I thank. I would also like to thank Dr. Hinde for first sparking my interest in programming as a senior, as well as molding my thinking about how to solve chemical problems using computers. Dr Hinde was also very gracious to spend time with me when I was having difficulty with the code for my thesis work. I would also like to thank Professor Adolfo Eguiluz for his inspirational Quanum Mechanics course in physics. His course had the most personal impact on

me than any other course I have participated. He emphatically encouraged students to think very deeply about the mysteries of quantum mechanics and he enabled his students to be able to actively "practice" quantum mechanics when they graduated. Without his course, I would not have had the tools to complete the theoretical part of this project. I would also like to extend thanks to the Department of Chemistry and The University for providing me the opportunity to earn a degree. Finally, I would like to thank all of the group members, past and present for the camaraderie we shared during my tenure. I wish you all everlasting health and happiness.

Science cannot solve the ultimate mystery of nature. And that is because, in the last analysis, we ourselves are a part of the mystery that we are trying to solve.

- Max Planck

Abstract

A MATLAB program was written to calculate the hindered rotational energies of the hydrogen and deuterium molecules interacting with an anisotropic potential, which may be thought of as a potential energy surface of a metal oxide substrate. It was found that an increase in the hindering potential of the rotation about the azimuthal angle lifted the degeneracy of the $j = 1, m_j$[magnetic quantum number] $= \pm$[plus or minus] 1 states. A better understanding of how the rotational states of these systems change as a function of the hindering potential can help to explain features in rotational inelastic neutron scattering spectra of hydrogen on ZnO. An attempt to produce single morphology zinc and magnesium oxide nanoparticles using a patented method by Larese and Kunnmann is discussed. The synthesis of magnesium oxide consistently produced single morphology MgO nanocubes. Zinc oxide synthesis produced a mixture of morphologies consisting of tetrapods, kites, and hexagonal pillars. The contents of the production cell were modified using a 50/50 graphite powder to chip ratio to decrease the diffusion rate of the metal vapor. Qualitative results suggest an increase in tetrapod concentration was realized via this modification.

Table of Contents

List of Tables

List of Figures

Chapter 1

Metal Oxides

Metal oxides in solid form have a well defined crystal structure. A crystal is described by an in infinite array of atoms, molecules, or ions that have a regularly defined geometric pattern. The structure of a crystal is best described by the crystal group basis vectors which define the unit dimensions within the crystal system Pauling (1930). All points in the lattice can be described by a linear combination of the basis vectors. In determining the unique structure of the crystal, the orientation of the various crystal planes is designated by Miller indices. These indices are a set of numbers designated h, k, l and relate the atomic positions in the crystal to the basis vectors of the crystal system (see fig 1.1). Magnesium oxide as synthesized in the Larese group has the (100) surface face exposed and can be prepared defect free. A scanning electron microscopy (SEM) image of some synthesized MgO cubes are shown in fig 1.2. MgO synthesized in the group can be successfully prepared without surface defects, although they are known to play an important role in determining the surface chemistry of oxides Scamehorn et al. (1994). The most common type of defects are the low coordinated Mg^{2+} and O^{2-} ions which are located on the edges or corners of the cube, as well as surface oxygen vacancies. A major concern during and after MgO production is the formation of hydroxyl groups on the surface. Hydroxyl groups form on the surface primarily due to the interaction of water molecules in humid air with the

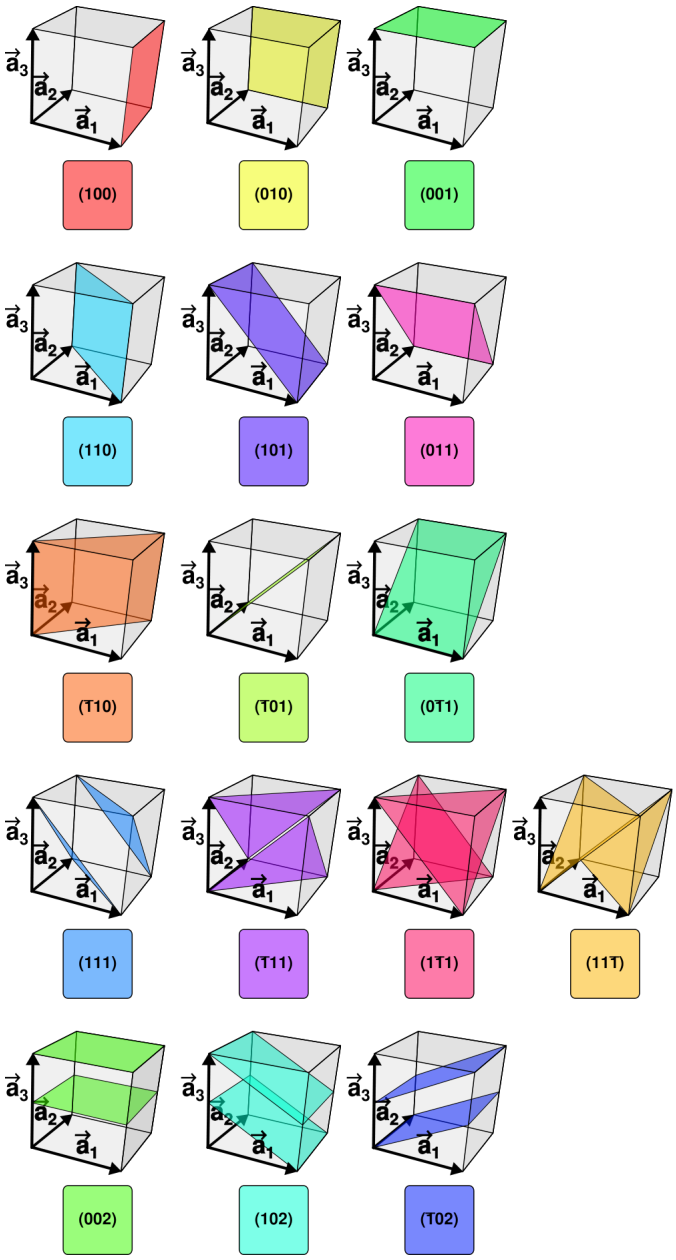

Figure 1.1: This figure shows the planes for the cubic lattice illustrating the usage of Miller indices. Miller indices enclosed with curved brackets (parentheses) refer to planes within the crystal. The vectors labeled $\vec{a}_1, \vec{a}_2, \vec{a}_3$, are the orthogonal basis vectors which define the cubic system. For MgO, the exposed facial plane is the (100) which is also equivalent to the (010) and (001).

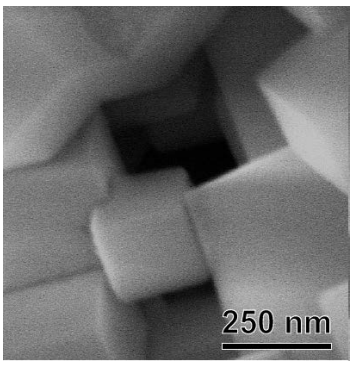

(a) This is an example of excellent quality MgO. The cubes are nearly perfect and the size distribution is small.

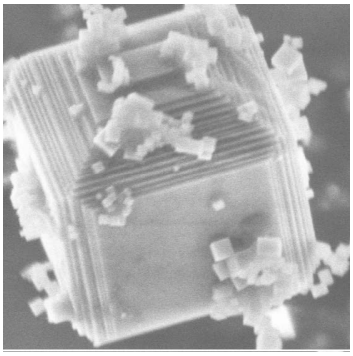

(b) This image is an example of poor quality MgO. Notice the stair case edges and the smaller surrounding cubes.

Figure 1.2: SEM images of MgO cubes of contrasting quality.

metal oxide surface. It has been shown that water readily undergoes surface catalyzed dissociative chemisorption Yu et al. (2003). Not only does this process hydroxylate the surface, it also has been shown to etch and destroy the low coordination sites much like a sugar cube dissolves in water. This process is detrimental to gas adsorption studies in which the surface should be as clean and defect free as possible to readily access the adsorption sites. To combat this process, the group synthesizes the oxides on low humidity days as monitored in the lab. Also a standard practice, the samples are kept in an inert environment inside a glove box or a desiccator.

1.1 Magnesium Oxide (MgO)

1.1.1 Experimental

The synthesis of MgO is outlined and discussed in detail in the Kunnmann and Larese patent Larese and Kunnmann (2001). Here, only a brief description of the synthesis is discussed with more important factors impacting the performance of the synthesis withheld for the quality control section.

Magnesium metal (approx 99.9% purity) is cut into small pieces and cleaned with

Figure 1.3: Image of the synthesis apparatus. The Lepel RF generator supplies power to the coil which inductively heats the graphite crucible and contents. Not shown are the gas tanks of argon and oxygen which are situated behind the generator.

dilute hydrochloric acid to remove any surface impurities. The principal impurity in the magnesium metal is manganese metal at ca. 4 ppm. The cleaned magnesium is mixed with high purity graphite and placed in a graphite crucible. The crucible is fabricated in the lab workshop using high quality graphite rods. After many production cycles the edges of the crucible become worn and a new crucible must be fabricated. The crucible is placed inside the coil of an induction furnace powered by a 6 kW RF generator. The crucible and coil are then covered by a large glass cylinder which is used to collect the resulting product. Once the atmosphere in the glass cylinder is displaced multiple times, the magnesium metal is heated inductively until the magnesium vapor begins to sublime and react with the graphite, forming highly reactive magnesium carbide. The magnesium carbide is thermally decomposed into carbon and magnesium vapors and subsequently reacted with oxygen, which is introduced into the growth chamber, resulting in the formation of highly pure,

nanometer scale cubes of magnesium oxide. This synthesis routine produces large quantities (ca. 20 g) of MgO powder that have a relatively narrow size distribution (250 ± 30 nm) as determined by SEM and TEM. The surface area of the particles is approximately 10 m^2g^{-1} as measured by a methane adsorption isotherm Freitag and Larese (2000).

It is has been found that exposure to the atmosphere for a significant amount of time degrades the adsorption properties of the sample. Exposure to air (especially humid air) is kept to a minimum throughout the production and sample preparation process. Immediately after synthesis, MgO samples are placed in a sealed desiccator, where they are stored until use. To prepare a sample for an adsorption study, the MgO is heated in a stepwise fashion to 950°C under high vacuum (10^{-7} torr) for a minimum of 36 hours. In addition to removing any atmospheric molecules physisorbed on the surface during and shortly after preparation, this heat treatment homogenizes the MgO (100) surface exposure Henrich and Cox (1994). Approximately 0.25 g of MgO is then loaded into an oxygen-free, high-conductivity (OFHC) copper cell under a dry argon atmosphere and sealed with indium wire.

1.1.2 Quality Control Procedures

The main goal of the MgO synthesis process is to produce single cubic morphology MgO powder with a very narrow particle size distribution with routine consistency. However, during the production process there are several variables that must be adjusted and monitored in order to ensure the highest quality product in the greatest yields. The most important parameters that will be discussed are the power ramp and duration, gas flow rates, the mass of the production cell, and the packing of the cell. There are two gas streams that are monitored and adjusted during the production cycle. One stream is ultra high purity argon and the other is oxygen. The flow rate of these streams are monitored via computer controlled flow-meters and can be adjusted at any time during the cycle. The argon stream is necessary for a variety of

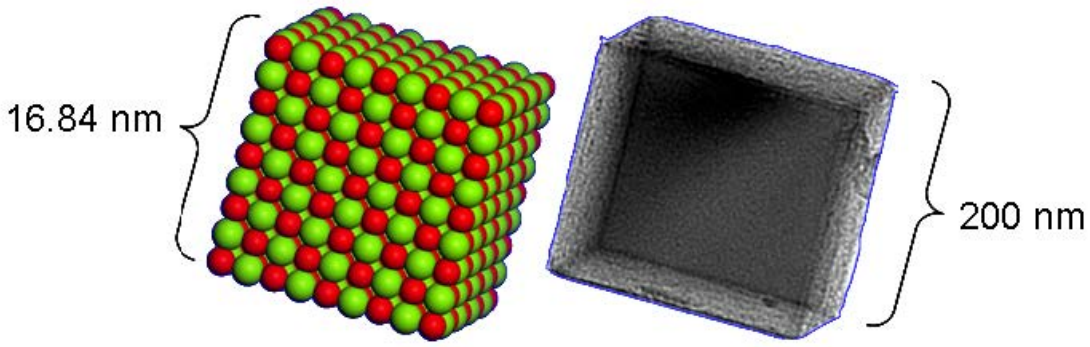

Figure 1.4: The cubic structure of MgO. In the model on the left, the magnesium atoms are green and the oxygen atoms are red. On the right is an actual image of an MgO cube

reasons, most which are outlined in Larese and Kunnmann (2001). The first is that prior to any production run, the glass collection cylinder is displaced multiple times with argon gas to ensure an inert environment that will not react with the metal vapor. The second is that it provides upward mobility and a chaotic environment which has been shown to increase metal vapor density that significantly narrows the particle size distribution Larese and Kunnmann (2001). However, the flow rate must be optimized because if too much is flowing too fast, it will have an adverse cooling effect on the vapor which often results in a decrease in yield. The production process is less sensitive to the flow rate of the oxygen. The only requirement is that the oxygen be present in excess and is generally switched on during the latter stages of the power ramp to prevent the reaction occurring at a less than optimal temperature.

The manufacturing station is powered by a high power radio frequency (RF) generator by Lepel. The power ramp is defined as the specific amount of power output over a certain duration of time. The RF generator has been configured for pre-defined set points which control the power output. During a production cycle, the power is set to low (set point 16) to allow the production cell to gradually increase in temperature to ensure uniform heating. After a variable period of time, usually when the top of the cell is uniformly reddish-orange the next and most **crucial** stage

in power ramping occurs. After the user has determined it is time to proceed with the reaction, the power is incremented by one or two set points until a wisp of vapor begins to evacuate the production cell. At this moment, the oxygen is turned on, and allowed to increase in volume inside the glass cylinder (10-20 seconds). Then, the ramp is most aggressive following the addition of oxygen by increasing the set point by one or two every 10 seconds or so until the reaction is initiated (visual burning). A critical point to note is that the exact timing of the power ramp is almost impossible to do using a timer. The user must keep close visuals on the production cell and make a judgment call on when to proceed higher. An improvement on the process would be to accurately measure the temperature of the cell perhaps using a temperature probe with a range exceeding 1100°C. If this is accomplished, the entire process could potentially be automated.

The production cell is comprised of a graphite crucible, small graphite chips, and magnesium metal cubes. Generally, the amount of pure metal cubes the crucible can hold is around 8-12 grams. The graphite chips serve as an interface and source of carbon to produce the magnesium carbide intermediate. The idea is to layer the magnesium with the graphite chips such that they reach the optimum reaction temperature before the metal-carbide exits the crucible. Therefore a layer of small graphite chips are placed on the bottom of the crucible followed by some of the magnesium cubes. The next layer consists of some of the medium sized graphite chips followed by another layer of magnesium cubes. The final layer consists of the largest graphite chips with some of the smaller chips saved over to fill the gaps. The reason the total mass of the production cell is important is because the greater the mass, the more power is required to heat it. Over time, the edges of the crucible become eroded as well as the chips themselves due to the reaction between the magnesium vapor and the graphite itself.

After production the product is weighed and prepared for quality testing via a methane adsorption isotherm. The collected product is prepared according to the process outlined in the experimental and a volumetric isotherm is performed on the

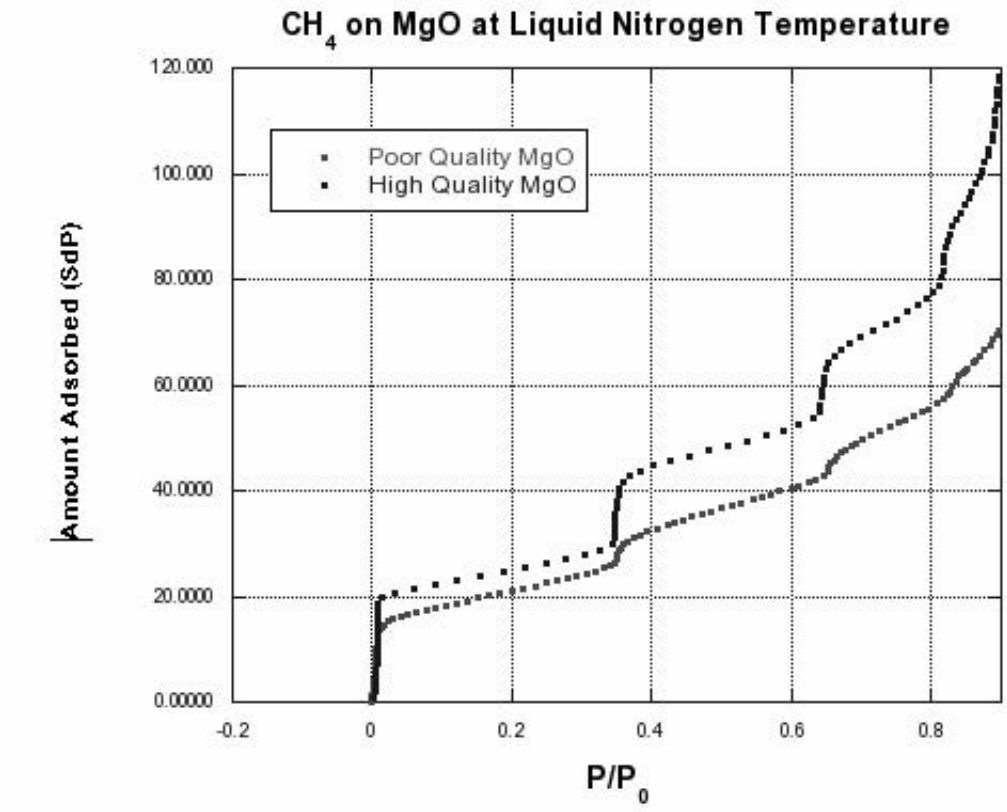

Figure 1.5: Adsorption isotherm comparing "high quality" and "low quality" MgO. Notice how the HQ MgO isotherm curve has symmetrical step heights and widths when compared to the LQ MgO.

sample. The adsorption isotherm of CH_4 on MgO has been studied in many papers by JZ. Larese and colleagues Freitag and Larese (2000) is the de facto standard of testing the quality of MgO. Other characterization methods such as X-ray diffraction or microscopy are also often used in tandem with the isotherm to confirm the quality of the oxide. However, these methods require instruments which are not immediately available in our laboratory so often the adsorption isotherm is used alone. The isotherm plot comparing high quality (HQ) and low quality (LQ) MgO is shown in fig. 1.5. Important factors in the analysis of the isotherm are the symmetry in the step heights and step widths, as well as the steepness (derivatives) of the steps themselves. High quality MgO would be characterized by extremely sharp and tall derivative peaks versus small broader peaks for the lower quality variety. After the batches of tested MgO have been analyzed they are sorted. The highest quality product is then placed in the glove box for use in neutron experiments or used as a framework for metal decoration. The lowest quality product is often discarded, with the medium quality kept for monolayer studies, student teaching, or for other non-critical experimentation.

1.2 Zinc Oxide (ZnO)

Zinc Oxide is a widely used industrial catalyst and can commonly be found as a component in paints, sunblock, the vulcanization of rubber, and as an anti-corrosion coating. ZnO is a post-transition II-IV metal oxide semiconductor with a direct bandgap of 3.37 eV and Wurtzite type crystal structure Van de Walle (2000). ZnO showcases several properties such as changes in electrical sensitivity, semiconducing, and optical properties which can depend on the type and concentration of defects, dopants, and adsorbed molecules. Those properties make it a useful material in additional applications including gas sensing, catalysis, and optoelectronic devices. ZnO is also often decorated with metal clusters of palladium, gold, and also silver. For example, nanowires made of ZnO have been considered as ideal building blocks for

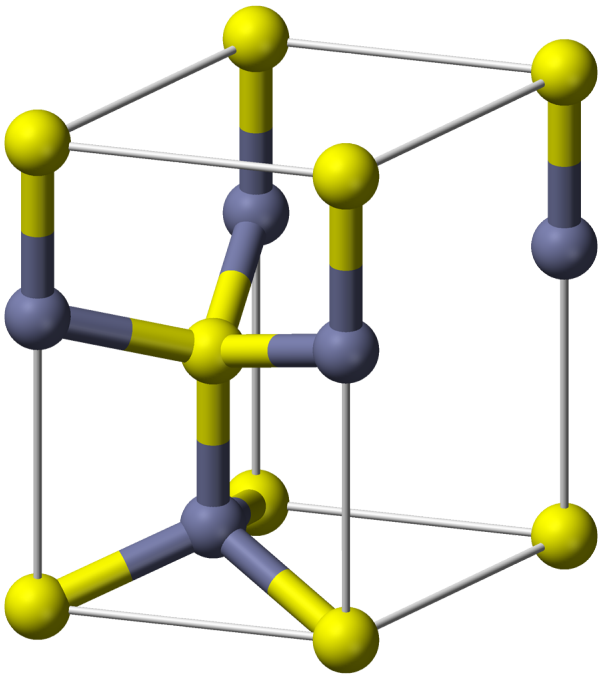

Figure 1.6: The Wurtzite structure of ZnO. The tetrahedral coordination of the metal is emphasized.

constructing nanowire sensors due to their high surface-to-volume ratio and the special physical and chemical properties originating from their size. Palladium decorated ZnO nanowires have been used for room temperature ethanol detection. Gold decorated ZnO has been shown to be an effective CO detector at room temperature Joshi et al. (2009). In the Larese group, the interaction of hydrogen with bare and metal decorated ZnO has been studied extensively.

1.2.1 ZnO Morphologies

Zinc oxide powder can be prepared in numerous morphologies (geometries) using a wide variety of synthesis techniques. The most frequently encountered and discussed are the tetrapods, hexagonal pillars, and needles. More rarely seen are the morphologies of nanoflower, nanonails, nanocarpets, nanokites, and nanosprings Wang (2004). Many of these structures can be homogeneously synthesized in small quantities on

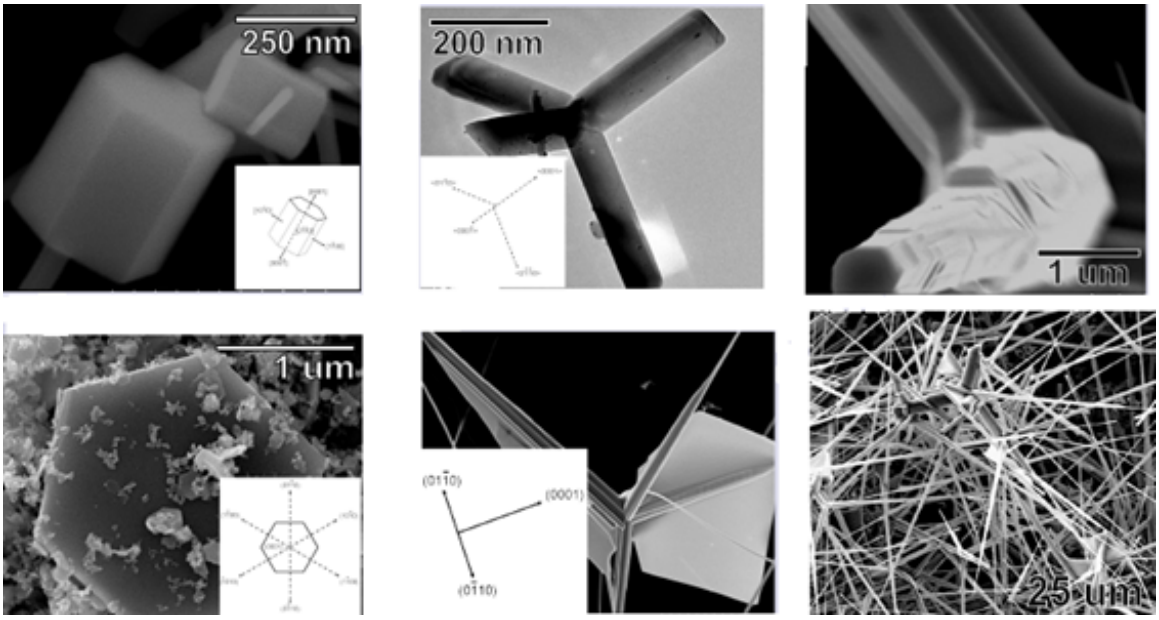

Figure 1.7: This figure illustrates some of the possible habitats or "morphologies" of zinc oxide nanoparticles raging from 200 nm to > 2 micron.

alumina substrates. A significant challenge is the synthesis of much larger quantities of ZnO with homogenous morphology throughout. In chemical vapor deposition synthesis, small changes in the flow of oxygen and argon, or modification of the composition of the source materials, lead to tetrapods with often different diameter legs Li et al. (2009). The wide array of structures that are possible suggests that even small changes in reaction conditions can significantly impact the synthesized product. We suspect that the temperature profile of the production cell (crucible, zinc metal, graphite chips) dictates the morphology of the ZnO nanoparticles.

1.3 Experimental

The synthesis for zinc oxide is nearly identical to the magnesium process described in the previous section. First, the boiling point of zinc is 1180 K compared to 1360 K for magnesium so the heating scheme will be different. Second, the pure zinc metal must be washed with dilute hydrochloric acid to remove any oxidation on the surface. The

synthesis process for MgO not as sensitive as ZnO as the cube is the most favorable (lowest energy) structure for this process. However, many more morphologies of ZnO are possible to generate with just small perturbations to the synthesis parameters. Group members have previously been able to produce single morphology nanoparticles consistently, however this knowledge and expertise departed as they did. The ability to find synthesis parameters (flow rates, masses, temperature) which consistently produce single morphology ZnO nanoparticles is the motivation for continuing this effort.

Several batches of ZnO were made using the procedure left by Dr. Paige Landry: Purge cylinder overnight, flush oxygen for 30 seconds before heating. Heat the cell for 5 minutes at set point 12. Turn on the oxygen flow, increase to set point 16 for 30 seconds. Repeat until set point 28 is reached. When the flame extinguishes, power down the RF generator but continue the oxygen flow. When no more product is being produced, shut off the oxygen, and keep the argon flowing to assist in cooling.

1.4 Results

It was suspected that if some ZnO vapor is escaping the crucible before the entire production cell has reached at least 900°C, the vapors will not have reacted at a uniform temperature which could explain the differences in morphologies and potentially reduce the yield. To combat this effect, some graphite chips were ground into a fine powder using a coffee bean grinder. The crucible was then filled with some of the graphite chips and zinc metal and covered with the graphite powder. The desired effect is to hinder the diffusion process by reducing the size of the gaps between the graphite chips so more zinc vapor is retained and allowed to heat uniformly. Samples of prepared ZnO were sent to Oak Ridge for SEM analysis. The images obtained from that analysis are shown in fig 1.6. In fig 1.6a, a mixture of tetrapods, kites, and hexagonal pillars can be seen. In fig 1.6b, the majority of the nanoparticles are in the tetrapod form with a few kites (top right) appearing. In fig 1.6c, once

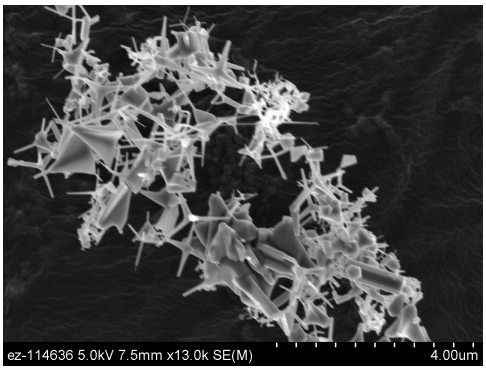

(a) SEM image of batch 0612A.

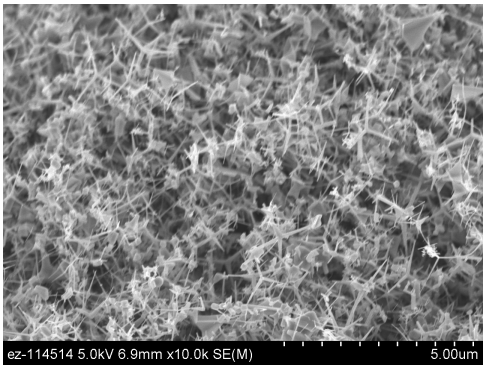

(b) SEM image of batch 0612B.

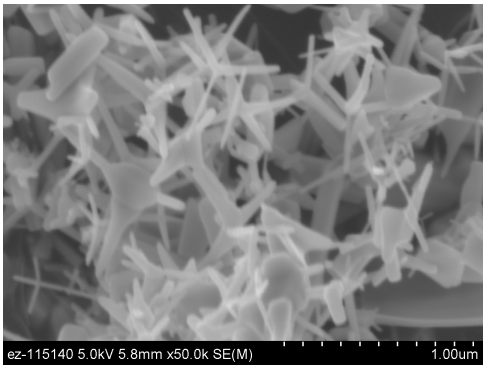

(c) SEM image of batch 0612C.

Figure 1.8: SEM images of different ZnO batches with varied argon flow rates. Samples were taken from the chimney.

Table 1.1: ZnO Synthesis Results

Batch	Ar Flow	O_2 Flow	Mass Zn	Notes	SEM Image
0612A	4%	15%	8.5 g	[a]	1.8a
0612B	5%	15%	9.0 g	[b]	1.8b
0612C	2%	15%	7.3 g	$\sim$	1.8c

[a] 0.5/0.5 graphite power and chip mixture
[b] 0.5/0.5 graphite power and chip mixture

again there is a mixture of morphologies however there is a definite visible increase in the concentration of tetrapods. Further testing with higher argon flow rates would be necessary to confirm this apparent pattern. The results via SEM could be coupled with X-ray diffraction, fluoroesce spectrometry, and neutron diffraction to provide more pathwasy of understanding how reaction parameters effect the pictures painted by those analytical techniques.

Chapter 2

Rotational Eigenstates of Molecular Hydrogen on Metal Oxide Surfaces

Hydrogen molecules (or dihydrogen) interacting with surfaces may behave similarly to free rotator hydrogen, dissociate into hydrogen atoms, or retain their molecular structure but undergo substantial electron transfer with the surface. Hydrogen dissociation is common when adsorbed on metal surfaces, and the separation of the hydrogen molecule into hydrogen atoms occurs at a distance of about 0.5Å. The hindered-rotation problem is an important topic in the study of the rotational spectrum of a molecule which is adsorbed on a solid surface. When a molecule is bound inside a crystal or adsorbed on a solid surface, owing to the molecule-molecule or molecule-surface interaction, the rotational motion of the molecule is generally hindered, and is energetically different from that of a free rotor. Therefore, a study of the states and energies of the hindered rotation is crucial to an understanding of the spectra of molecules and molecular crystals, and also the dynamics of adsorption and desorption. The first evidence of hindered rotations of an adsorbed molecule on a surface was the observation of ortho-para separation factors of the adsorbed

hydrogen and deuterium Sandler (1954). It is therefore the main motivation to be able to computationally predict the splitting of rotational states as a function of rotational barrier strength in such systems.

2.0.1 The Spin Isomers of Hydrogen

A consequence of the quantum mechanical restrictions on the symmetry of the rotational functions of molecular hydrogen provide two distinct spin isomers of H_2. These species are referred to as "ortho-" and "para-" hydrogen. The hydrogen nucleus, composed of a single proton with half-integer nuclear spin, is a fermion. As a consequence, the quantum mechanical description of fermions must obey Fermi-Dirac statistics. In the case of dihydrogen, the nuclei are indistinguishable and upon their interchange, the parity of the total wavefunction must change sign. The total wavefunction is separable into a rotational function: $Y_{jm}(\theta, \phi)$ and nuclear spin function: ψ_{spin}. Therefore, the permutation operator hitting the total wavefunction must flip the sign of the total wavefunction as required by Fermi statistics:

$$\hat{P}_{12}\psi_{total} = (-1)Y_{jm}(\theta, \phi)\psi_{spin} \tag{2.1}$$

The physical representation of this operation is the C_2 rotation about the axis normal to the H-H bond. The symmetry of the rotational wavefunction under such exchange is:

$$Y_{jm}(\pi - \theta, \pi + \phi) = (-1)^j \; Y_{jm}(\theta, \phi) \tag{2.2}$$

And the spin functions are:

$$\psi_{spin}^{sym} = \begin{cases} |{+}{+}\rangle \\ |{-}{-}\rangle \\ \frac{1}{\sqrt{2}}\left(|{+}{-}\rangle + |{-}{+}\rangle\right) \end{cases} \qquad \psi_{spin}^{asym} = \left\{ \frac{1}{\sqrt{2}}\left(|{+}{-}\rangle - |{-}{+}\rangle\right) \right. \tag{2.3}$$

$|+\rangle$ corresponds to the projection of the angular momentum onto the z-axis with eigenvalue $\frac{\hbar}{2}$ and the ket $|-\rangle$ corresponds to the projection of the angular momentum onto the z-axis with eigenvalue $-\frac{\hbar}{2}$. The even values of j ("p-") correspond to symmetric rotational functions and therefore must be multiplied with antisymmetric spin functions to form an antisymmetric total wavefunction. The only allowed rotational states of spin paired or antiparallel dihydrogen are those with $j = 0, 2, 4, \ldots$. The odd values of j ("o-"), $j = 1, 3, 5, \ldots$, correspond to antisymmetric rotational functions and therefore must be multiplied with symmetric spin functions (to form an antisymmetric total wavefunction.) Molecules of hydrogen occupying different rotational energy levels have been shown to exhibit different physical properties. The ratio between the ortho and para hydrogen is approximately 3:1 at STP which is a direct reflection of the ratio of the spin degeneracies and the mixture is referred to as normal hydrogen. However, if thermal equilibrium is achieved, the para (ground state) dominates at low temperatures (99.8% at 20 K). In the absence of a catalyst, transitions between the spin paired and unpaired states are "spin trapped". While the rotational ground state energy is zero, the minimum energy of the first ortho level is $2B_{rot}$, where $B_{rot} = 59.3\ cm^{-1}$ is the rotational constant for dihydrogen.

2.1 Inelastic Neutron Scattering

The pure rotational transitions of symmetrical diatomic molecules like dihydrogen are forbidden in infrared spectroscopy by the dipole selection rule but are active in Raman spectroscopy due to the allowed change in polarizability Cotton (1990). Rotations are, in principle, observable in INS due to the lack of selection rules, but the scattering is generally weak except for dihydrogen due to the large incoherent scattering cross section. As a result, using INS to study dihydrogen and its local environment is often advantageous and the experimental technique of choice.

Studies of the rotational behavior of hydrogen and deuterium adsorbed on graphite and magnesium oxide have been done previously Larese et al. (2009). These studies

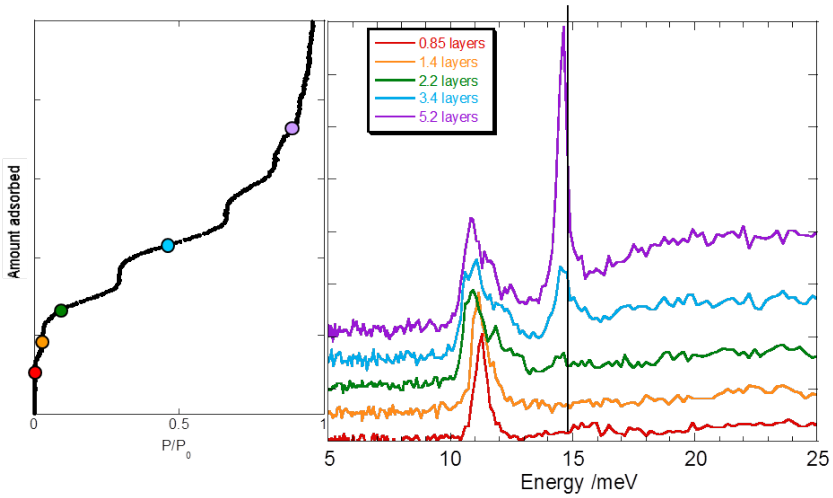

(a)

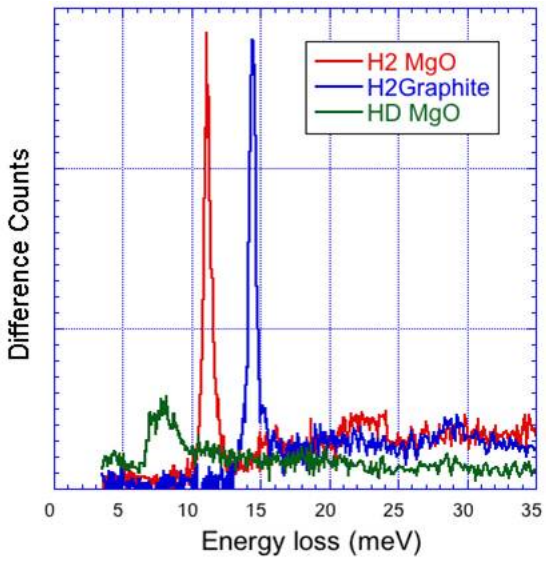

(b)

Figure 2.1: (a) INS spectrum of the multilayer H_2 film adsorbed on MgO (100) nanocubes ca. 10K. (b) INS spectrum recorded at ∼10 K illustrating the behavior of the j = 0 to the j = 1 O to P transition for an adsorbed H_2 monolayer film on graphite (blue trace), MgO(100) (red trace), and a monolayer HD film adsorbed on MgO(100) (green trace). The excitation located at ca. 14.7 meV is located at the same place as this transition in bulk H_2 (free rotor). Image credit Larese et al. (2009)

showd that INS techniques are exceptionally well suited to monitor the changes in the barrier to molecular rotation as a function of the layer thickness of the adsorbed molecules. In figure 2.1a, the dependence of the INS response to film coverage is illustrated. Below a monolayer of coverage, the response at 11.3 meV corresponds to hydrogen molecules whose strong interaction with the MgO surface hinders the rotation, thereby causing a decrease in the j = 0 to 1 rotational transition energy. Recall that a lower barrier to rotation increases the j = 0 to 1 rotational energy, causing an upfield shift in the INS spectrum. Above 2.2 layers, an upfield shoulder appears off the 11.3 meV response and this was shown to be due to the displacement of molecules off of the Mg cation sites which resulted in a reduction in the hindering potential for some of the molecules withing the film. Above 3.4 layers of coverage, a new response appears at approximately 15 meV and increases in intensity as coverage increases. This is due to the increased molecule-molecule interactions which predominately determine the dynamical properties of the adlayer farthest from the surface. This would suggest that the dynamics of the upper adlayers is closely related to the bulk system due to the increased distance from the surface. Multilayer films need to be at least 2 to 3 layers thick before any molecules within the layers will experience molecule-molecule interactions more strongly than the molecule-surface interactions. In figure 2.1b, INS spectrum of monolayer adsorbed dihydrogen on MgO and graphite. It was found that bulk dihydrogen molecules adsorbed on the basal plane of graphite behaves as a free rotator with the ortho to para transition occurring at ∼14.7 meV Larese et al. (2009). Tying in the results from figure 2.1a, we once again see the 11.3 meV response from the single adlayer of hydrogen on MgO. However when deuterium is substituted for a single hydrogen to form HD, the peak shifts lower in energy due to the smaller rotational constant.

In figure 2.2, the predominant feature at ∼14.7 meV appears once again as the graphite surface does not have any appreciable effect on the rotational energies of monolayer adsorbed hydrogen molecules. However, when the substrate is swapped for graphite nanohorns, the peak is broadened symmetrically on either side. If one

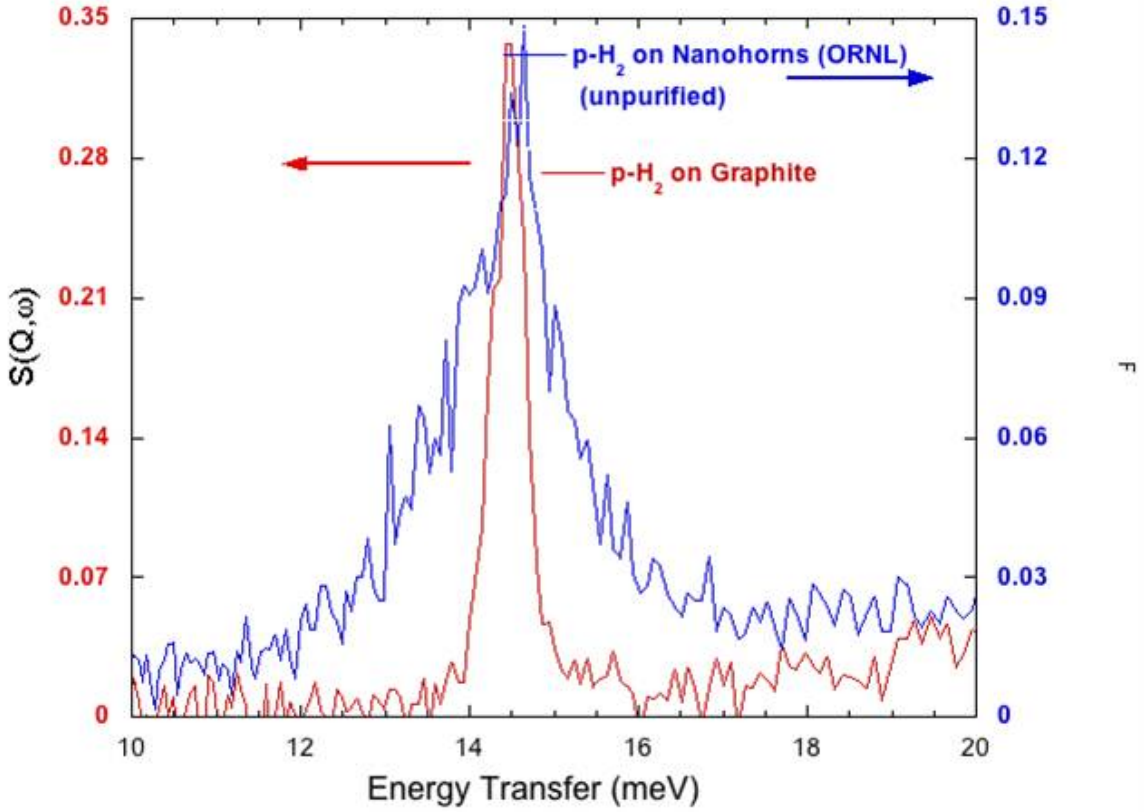

Figure 2.2: INS spectrum of monolayer hydrogen molecules adsorbed on graphite and carbon nanohorns.

integrates the two peak areas, the peak at 14.7 from the hydrogen molecules adsorbed on the nanohorn substrate has approximately three times the area of the peak from the vanilla graphite. This broadening could be as a result of the nanohorn substrate hindering the rotation of the hydrogen molecules resulting in a splitting of the j = 1 state.

2.2 The Two Particle Linear Rigid-Rotor

The two-particle rigid rotor problem is a very special case in quantum mechanics as it is one of the handful of problems which can be solved exactly. The formalism developed here lays the foundation for the later work in describing the hindered rotation of the hydrogen molecule. The two-particle rigid rotor is a system composed of two particles at some fixed distance from each other of length d, with the center of mass at some position $\vec{R}$ from the origin. Therefore, the only contribution to the kinetic energy is rotational motion. If the total energy of the rotor is completely kinetic, then it must follow that:

$$V(\vec{R}) = 0. \tag{2.4}$$

The Hamiltonian for this system reduces to:

$$\hat{H} = \frac{\hat{p}^2}{2\mu} = -\frac{\hbar^2}{2\mu}\nabla^2. \tag{2.5}$$

$$\mu = \frac{m_1 m_2}{m_1 + m_2}. \tag{2.6}$$

Where μ is the reduced mass and ∇ is the Laplacian. Therefore, the total Hamiltonian in spherical coordinates is:

$$\hat{H} = -\frac{\hbar^2}{2\mu}\left[\frac{1}{r^2}\frac{\partial}{\partial\, r}\left(r^2\frac{\partial}{\partial\, r}\right) + \frac{1}{r^2}\frac{1}{sin\ \theta}\frac{\partial}{\partial\theta}\left(sin\theta\frac{\partial}{\partial\theta}\right) + \frac{1}{r^2\ sin^2\theta}\frac{\partial^2}{\partial\phi^2}\right]. \tag{2.7}$$

This equation assumes that the intermolecular distance r is not fixed. Since, in the rigid rotator approximation the intermolecular distance is fixed, we have the Hamiltonian:

$$\hat{H} = -\frac{\hbar^2}{2I}\left[\frac{1}{sin\ \theta}\frac{\partial}{\partial\theta}\left(sin\theta\frac{\partial}{\partial\theta}\right) + \frac{1}{sin^2\theta}\frac{\partial^2}{\partial\phi^2}\right]. \tag{2.8}$$

Where I is the moment of inertia defined as $I = \mu d^2$ and r = 1. Now, to find the energy levels for this system we must solve the eigenvalue problem:

$$\hat{H}\Psi(\theta,\phi) = E\Psi(\theta,\phi). \tag{2.9}$$

Such that $\Psi(\theta,\phi)$ are the eigenfunctions of $\hat{H}$. By utilizing separation of variables, Ψ can be separated into a product of functions of θ and ϕ.

$$\Psi(\theta,\phi) = \Theta(\theta)\Phi(\phi). \tag{2.10}$$

Substituting Eq. 2.7 and Eq. 2.10 into Eq. 2.9 and dividing through by $\Theta(\theta)\Phi(\phi)$ yields:

$$\frac{sin\ \theta}{\Theta(\theta)}\frac{\partial}{\partial\theta}\left[sin\ \theta\frac{\partial\Theta(\theta)}{\partial\theta}\right] + \frac{2IE}{\hbar^2} = -\frac{1}{\Phi}\frac{\partial^2\Phi}{\partial\phi^2} \tag{2.11}$$

Since both sides of the equation must be equal up to a constant designated m^2, Eq. 2.11 yields two differential equations:

$$\frac{d^2\Phi(\phi)}{d\phi^2} = -m^2\Phi(\phi) \tag{2.12}$$

$$\frac{1}{sin\ \theta}\frac{\partial}{\partial\theta}sin\ \theta\frac{\partial\Theta(\theta)}{\partial\theta} - \frac{m^2}{sin^2\ \theta}\Theta(\theta) + j(j+1)\Theta(\theta) = 0 \tag{2.13}$$

Where the constants involving E have been replaced by $j(j+1)$. Eq. 2.12 has the normalized solutions

$$\phi_m(\theta) = \frac{e^{\imath m\phi}}{\sqrt{2\pi}} \quad m = 0, \pm1, \pm2, \ldots \tag{2.14}$$

The normalized solutions for $\Theta(\theta)$ are the normalized associated Legendre polynomials

$$\Theta_{j,m}(\theta) = \sqrt{\left[\frac{2j+1}{2}\frac{(j-m)!}{(j+m)!}\right]} P_j^m(cos\theta). \tag{2.15}$$

and (2.9) has allowed solutions only for integer values of $j, j \geq \mid m \mid$. The associated Legendre polynomials, $P_j^m(cos\theta)$ are defined as

$$P_j^m(\xi) = (1-\xi)^{\frac{m}{2}} \frac{\partial^m}{\partial \xi^m} P_j(\xi),\ \xi = cos\ \theta. \tag{2.16}$$

The $P_j(\xi)$ are the Legendre polynomials defined by the series expansion

$$P_j(\xi) = \frac{1}{2^j} \sum_{n=0}^{\frac{j}{2}} (-1)^n \begin{pmatrix} j \\ n \end{pmatrix} \begin{pmatrix} 2j-2n \\ j \end{pmatrix} \xi^{j-2n} \tag{2.17}$$

where

$$\begin{pmatrix} j \\ n \end{pmatrix} = \frac{j!}{n!(j-n)!} \tag{2.18}$$

The restriction that j must be a positive integer implies that only the energies,

$$E = \frac{\hbar^2}{2I} j(j+1), j = 0, 1, 2, \ldots \tag{2.19}$$

are allowed for the rigid rotor. There are therefore $2j+1$ degenerate states since for any j, $m = -j, -j+1, \ldots, 0, j+1, j+2, \ldots$ The total wavefunction is now the product of the Φ and Θ parts which is finally,

$$\Psi(\theta, \phi) = \Theta(\theta)\Phi(\phi) = Y_j^m(\theta, \phi). \tag{2.20}$$

The functions $Y_j^m(\theta, \phi)$ are known as the spherical harmonics and form a complete, orthonormal basis in state space ξ:

$$\langle j', m' \mid j, m \rangle = \delta_{m,m'}\ \delta_{l,l'} \tag{2.21}$$

With closure relation:

$$\sum_{j=0} \sum_{m=-j}^{j} |j,m\rangle \langle j,m| = \hat{1}. \tag{2.22}$$

It therefore follows that the eigenvalue problem for the rigid rotator is:

$$\hat{H}\ Y_j^m(\theta,\phi) = \frac{\hbar^2}{2I}\ j(j+1)\ Y_j^m(\theta,\phi) \tag{2.23}$$

2.2.1 Quantum Matrix Mechanics

It is proven that the Laplace spherical harmonics form a complete, orthonormal set of functions and thus form an orthronormal basis of the state space ξ of square-integrable functions. On the unit sphere, any square-integrable function can be expanded as a linear combination of these. Let $|\chi\rangle$ be an eigenvector of the perturbed Hamiltonian, $\hat{H}'$. The expansion of $|\chi\rangle$ in the basis of the spherical harmonics therefore becomes:

$$|\chi\rangle = \sum_{j} \sum_{m=-j}^{j} C_{\chi,jm}\, |jm\rangle \tag{2.24}$$

Once these coefficients have been found via the traditional matrix diagonalization method, we know everything about the state space of the perturbed Hamiltonian. This means that we can calculate the full spectrum of energies. Now, let us derive eigenvalue equation for the perturbed Hamiltonian in the basis of the spherical harmonics. The eigenvalue problem becomes:

$$\hat{H}'\,|\chi\rangle = E'\,|\chi\rangle \tag{2.25}$$

Project on the left with $\langle j'm'|$:

$$\left\langle j'm' \,\middle|\, \hat{H}' \,\middle|\, \chi \right\rangle = E'\,\langle j'm'\,|\,\chi\rangle \tag{2.26}$$

Invoke the closure relation:

$$\left\langle j'm' \left| \hat{H}'\hat{1} \right| \chi \right\rangle = \sum_{j} \sum_{m=-j}^{j} \left\langle j'm' \left| \hat{H} \right| jm \right\rangle \langle jm \,|\, \chi \rangle = E' \langle j'm' \,|\, \chi \rangle \tag{2.27}$$

$$\sum_{j} \sum_{m=-j}^{j} C_{jm} \left\langle j'm' \left| \hat{H} \right| jm \right\rangle = E' \; C_{j'm'} \tag{2.28}$$

$$\sum_{j} \sum_{m=-j}^{j} C_{jm} \hat{H}_{jj'mm'} - E' \; C_{j'm'} = 0 \tag{2.29}$$

$$\sum_{j} \sum_{m=-j}^{j} \left(\hat{H}_{jj'mm'} - E' \delta_{jj'} \delta_{mm'} \right) C_{jm} = 0 \tag{2.30}$$

Now, the eigenvalue equation in abstract space has been transformed into a homogeneous linear matrix equation for the expansion coefficients C_{jm}. But first, we must know the representation of the perturbed Hamiltonian in the basis of the spherical harmonics. The representation of this operator in the basis of the spherical harmonics can be written

$$\left\langle j'm' \left| \hat{H}' \right| jm \right\rangle = \frac{\hbar^2}{2I} \; j(j+1)\delta jj'\delta mm' + \lambda \langle j'm' \,|\, V(\theta,\phi) \,|\, jm \rangle \tag{2.31}$$

The first part of the matrix element is the kinetic energy and only depends on j. The second part of the matrix element is the integral:

$$\langle j'm' \,|\, V(\theta,\phi) \,|\, jm \rangle = \int_{\Omega_2} Y^*_{jm} Y_{j'm'} \; V(\theta,\phi) d\Omega_2 \tag{2.32}$$

Where $d\Omega_2 = sin(\theta) \; d\theta \; d\phi$. Once these integrals are computed, the matrix $\hat{H}_{jj'mm'}$ can be fully constructed and the matrix equations from Eq. 2.26 can be solved.

2.2.2 Quadrature on the 2-Sphere

The integrals needed to compute the matrix elements of the perturbed Hamiltonian are evaluated numerically using Lebedev quadrature Lebedev (1976). The surface integral of some $f(\theta, \phi)$ over the 2-sphere,

$$I_{exact} = \frac{1}{4\pi} \int_{\Omega_2} d\Omega_2 f(\Omega_2) \tag{2.33}$$

may be approximated via Lebedev quadrature as:

$$I_{approx} = \sum_{i=1}^{N} w_i f(\phi_i, \theta_i) \tag{2.34}$$

The quadrature scheme (and the number of points, N) is chosen to make the approximation via quadrature of all overlap integrals intact. In density functional theory, it is common to calculate the exchange, correlation, and kinetic energy corrections to the energy by summing contributions from 3D cells centered on each of the nuclei Wang and Carrington (2003). The angular part of these 3D integrals, (θ, ϕ), is generally computed using the Lebedev quadrature Becke (1988). Using Lebedev points it is possible to compute exactly:

$$\int_0^{\pi} sin(\theta) d\theta \int_{-\pi}^{\pi} d\phi \; Y_{lm}(\theta, \phi) \tag{2.35}$$

for $\ell = 0,\ldots,$L with approximately

$$\frac{(L+1)^2}{3} \tag{2.36}$$

points Wang and Carrington (2003). Lebedev points and weights are available for values of L (called the order of the grid) as large as 131. To do all of the spherical

harmonic integrals correctly, one needs a quadrature order $L = 2\ell_{max}$ and therefore

$$N_{leb} = \frac{4}{3}(\ell_{max} + 1)^2 \tag{2.37}$$

points versus,

$$N_{GL} = 2(\ell_{max} + 1)^2 \tag{2.38}$$

for the Gauss-Legendre scheme. What makes the Lebedev scheme attractive versus

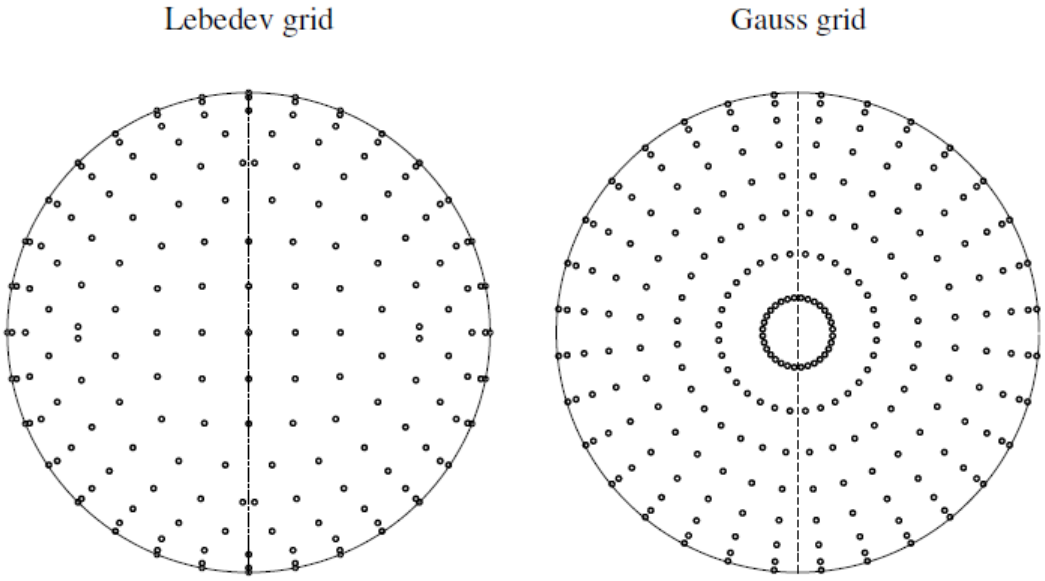

Figure 2.3: The sphere on the left side shows the Lebedev grid with 350 points and on the right side, the Gauss grid with 512 points. Notice how on the Lebedev grid, the points are equally spaced over the surface, and the Gauss grid has more points accumulating at the poles.

the Gauss-Legendre scheme is that the number of points required for the overlap integrals to be computed correctly is 1.5 times smaller than the Gauss grid. A subroutine which contained the weights and points for the Lebedev quadrature was used thanks to Rob Parrish, The Sherrill Group, CCMST Georgia Tech.

2.3 The hindered rotational eigenstates of H_2 and D_2

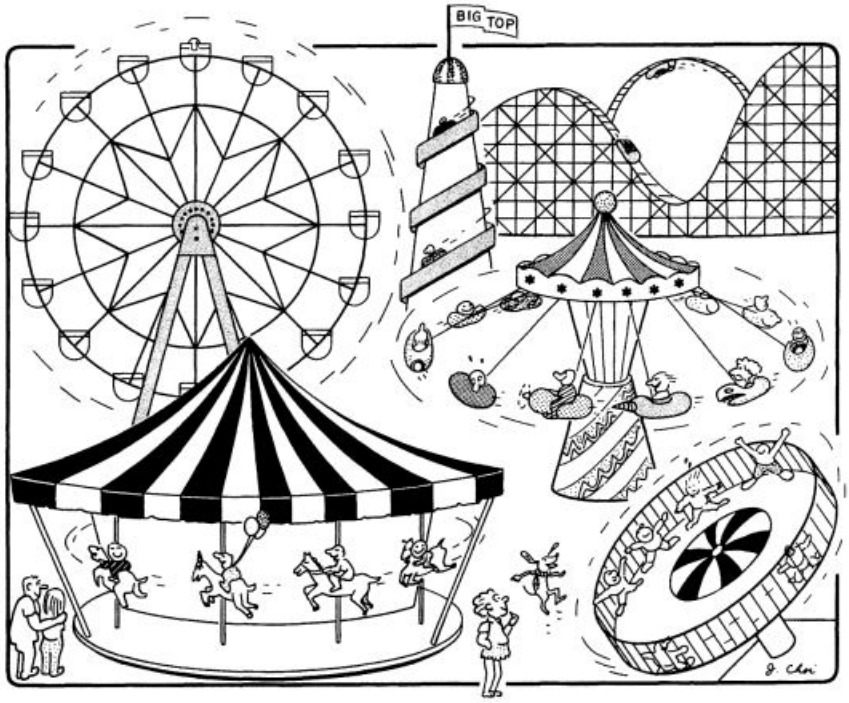

2.3.1 A 1D Hindering Potential: $V(\theta, \phi) = cos^2(\theta)$

As a fan of amusement parks, I have often enjoyed my fair share of ferris wheels, carousels, and merry go rounds. On the macroscopic level, it is quite easy for us to see and feel angular momentum at work. Whether it be the centrifugal force trying to dismount you from the carousel horse, or the heavy feeling you get during an ascent of the Ferris wheel. Very few of us think about how the Ferris wheel and the carousel rotate in one dimension, in perpendicular planes. Better yet, the tilt-a-whirl, which can be seen in the lowest right hand corner in the cartoon rotates in two dimensions. However, when we take these macroscopic ideas down to the quantum level, we learn that the operator of these rides cannot choose a continuum of energies to run at, but only discrete ones. In this study we will try to visualize and understand the

interaction of dihydrogen with a few simple potentials. This is particularly useful when studying the perturbed rotational states of hydrogen adsorbed on metal oxide surfaces, as these can be probed using neutron spectroscopy. The complexity lies when attempting to assign transitions to the observed peaks in the experimental spectrum. By calculating a few known transitions from the experimental spectra, one can hope to tune the barrier strength parameters (explained below) so that the program can calculate energies which are in reasonable agreement with experiment. From there, the user can get energies of other transitions from the program which can be used to label unknown transitions in the experimental neutron spectra. First, let us consider a system in which non-interacting diatomic molecules are physically adsorbed on an adsorbent which hinders the out-of-plane rotation of the adsorbed molecules. The adsorption may be either mobile or localized. The adsorbent is taken to be a continuous plane with the adsorbed diatomics at an equilibrium distance Z from the surface (adsorbent) MacRury (1969). This distance must be greater than the length of the diatomic molecule so that at the limit of zero hindrance, the molecule behaves as a free rotator much like the ferris wheel in the figure above (in the limit of zero air resistance, even load distribution, and frictionless bearings). The angle θ is defined as the angle between the z-axis, which is perpendicular to the surface and passes through the center of mass of the diatomic, and the molecular axis of the diatomic. Therefore, a hindering potential of the form

$$V(\theta) = \lambda \; cos^2(\theta) \tag{2.39}$$

where lambda is the barrier height of the out of plane rotation. This potential is an acceptable model for the "ferris wheel" because it goes through a maximum when $\theta = n\pi$, i.e. when the molecule is orthogonal to the xy-plane and through a minimum when $\theta = \frac{n\pi}{2}$ i.e. when the molecule is parallel to the surface (see Fig. 2.4). The ϕ angle is unhindered by the model (Fig. 2.5) and so this angle is defined as the angle between some reference plane passing through the z axis and a plane passing through

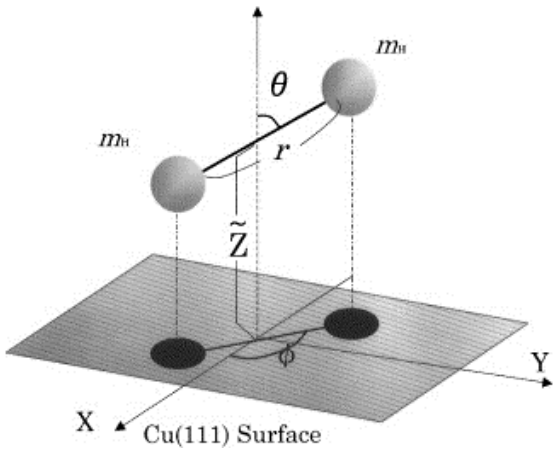

Figure 2.4: The model system for dihydrogen with the center of mass distance to the surface Z, molecular bond length r, polar angle θ, and azimuthal angle ϕ. Miura et al. (1999) with written permission from Elsevier.

the z axis and molecular axis Macrury and Sams (1970).

In order to obtain the rotational eigenstates and eigenenergies of an adsorbed molecule hindered by the potential given in Eq. 2.39 is is necessary to solve the Schrödinger equation as shown in Eq. 2.9. Where this time the potential component of the Hamiltonian is nonzero in contrast to the free rotator. The Hamiltonian for this system now forms the perturbed Hamiltonian and becomes:

$$\hat{H}' = \hat{T} + \hat{V} \tag{2.40}$$

and substituting for the kinetic energy and potential energy operators:

$$\hat{H}' = \frac{\hbar^2}{2I}\, j(j+1) + \lambda\, cos^2(\theta) \tag{2.41}$$

Where the kinetic energy portion originates from motion of the free rotator and I is the moment of inertia. The matrix elements of the perturbed Hamiltonian in the basis of the spherical harmonics are now given by:

$$\left\langle j'm' \middle| \hat{H}' \middle| jm \right\rangle = \frac{\hbar^2}{2I}\, j(j+1)\delta jj'\delta mm' + \lambda \left\langle j'm' \middle| cos^2(\theta) \middle| jm \right\rangle \tag{2.42}$$

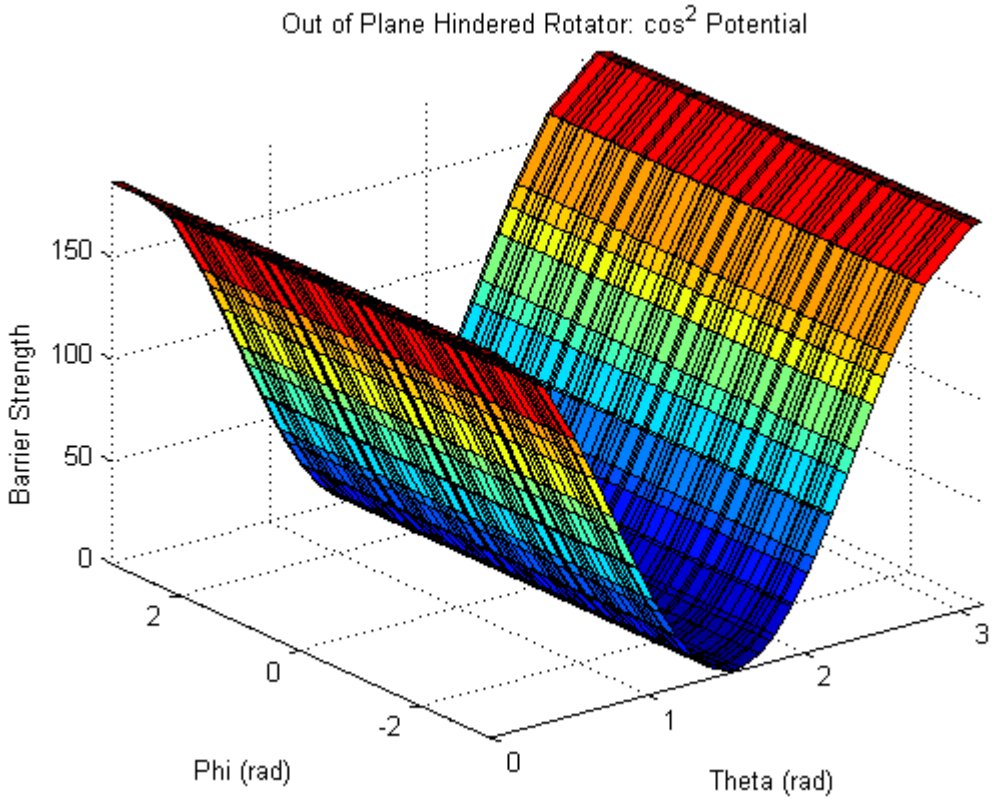

Figure 2.5: The functional form of the out of plane hindered rotator. The azimuthal angle ϕ is unhindered by this potential and so the potential remains constant. The potential goes through maxima at integer values of π and minima when $\theta = \frac{n\pi}{2}$ i.e. when the molecule is parallel to the surface.

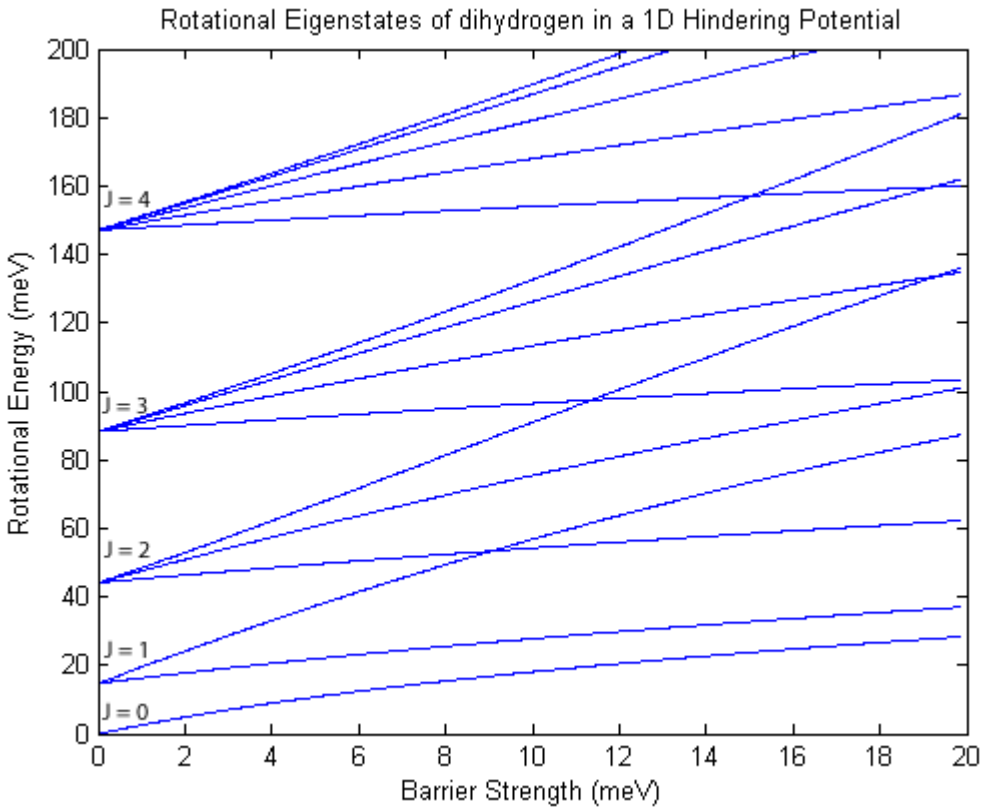

Figure 2.6: Energy level diagram for the 1D (out-of-plane hindered rotor). The energies are plotted as a function of the barrier strength which varies from 0 to 20 meV. Since the rotation about the azimuthal angle ϕ is not hindered by this potential, the degeneracies in the m_j states are not lifted.

Using a basis of 64 spherical harmonics ($j = 7$ to minimize error), the matrix elements of this Hamiltonian are calculated (86 Lebedev points) and the resulting matrix eigendecomposed using MATLAB built-in subroutines. The energies up to j = 4 as a function of the 1D barrier height are plotted in 2.6, but 64 rotational states are available. When the barrier strength parameter is approximately 0, the energies collapse to the free rotor states. Since the rotation about the azimuthal angle ϕ is not hindered, the degeneracies in the $\pm m$ states are not raised, only the $2j + 1$ degeneracies are. As the barrier strength approaches 9 meV, a level crossing occurs between the $|1 \pm 1\rangle$ and the $|20\rangle$ states. These states were calculated using the script which utilized Clebsch-Gordan coefficients to calculate the integrals (see appendix).

As the barrier strength increases, the potential is most attractive when the molecule lies parallel to the surface. These rotational states are represented by the planar, ring-doughnut $|1 \pm 1\rangle$ states.

2.3.2 A More Representative Potential

The direction of the anisotropic potential is now taken to lie along the z-axis, normal to the surface. A common situation occurs for dihydrogen adsorbed onto a surface where the x- and y-axis are defined in the plane of the surface. As the out-of-plane forces along the z-axis, securing the molecule to the surface increase in strength, the rotational states near the surface are perturbed White and Lassettre (1960). Consider a potential of the form:

$$V(\theta, \phi) = \left[a + \frac{b}{2}\ cos(2\phi)\right]\ sin^2(\theta) \tag{2.43}$$

where θ is the polar angle (the angle between the H-H bond and the surface), ϕ is the azimuthal angle (between the x-axis, defined to be in the plane of the surface, and the projection of the H-H bond onto the surface plane). The values of a and b give relative weights of the potential and the factor of two in the cosine term represents how the symmetry of the field matches the C_2 molecular symmetry of dihydrogen.

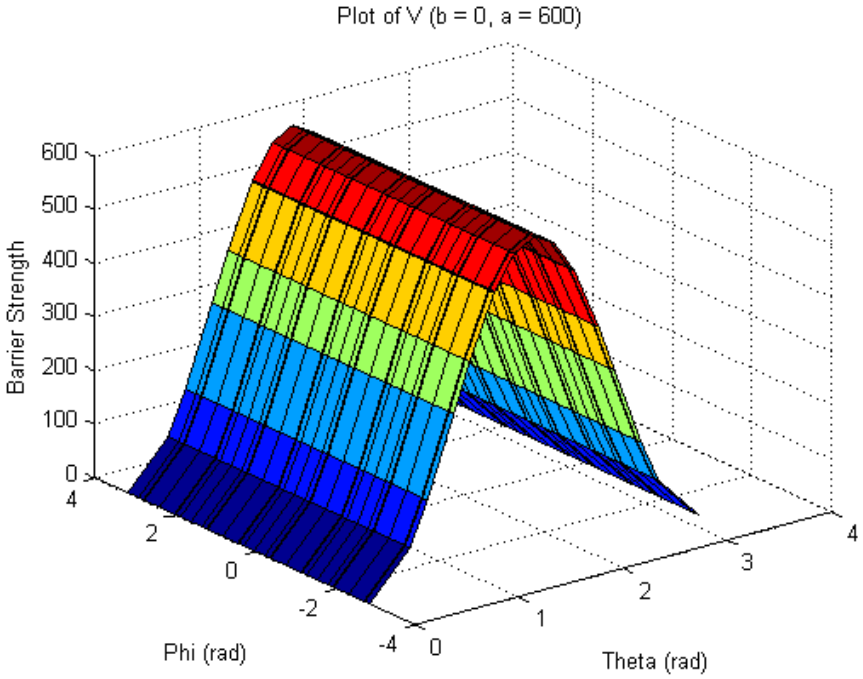

(a) When $a > 0$, the potential is most attractive when the molecular axis is orthogonal to the surface. The potential is invariant upon rotation about the azimuth.

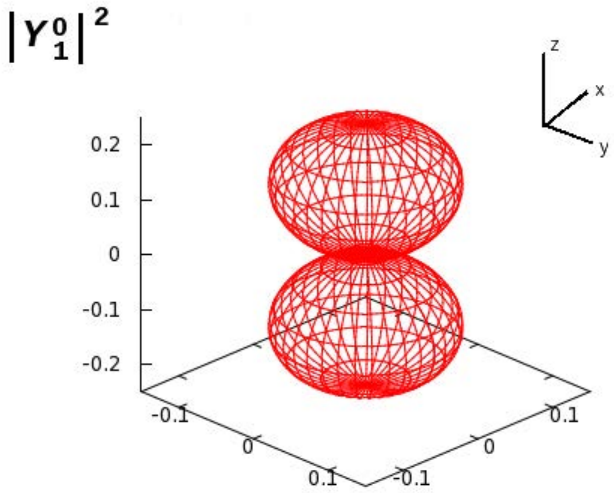

(b) The "p" type spherical harmonic.

Figure 2.7: The probability density of the dumbell shaped state which is stabilized by the potential with negative values of a, b ~ 0.

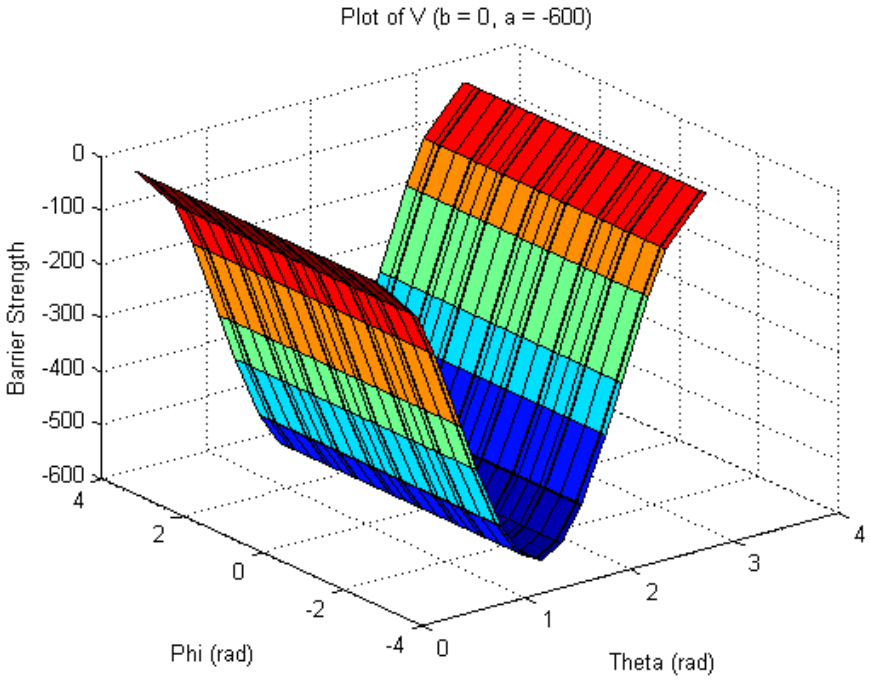

(a) When $a < 0$, the potential is most attractive when the molecular axis is parallel to the surface. The potential is invariant upon rotation about the azimuth.

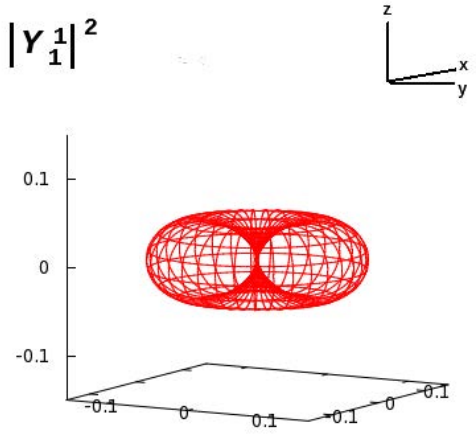

(b) The probability density of the degenerate $|1 \pm 1\rangle$ torus shaped state. One could generate this state by rotating the $|10\rangle$ state $\frac{\pi}{2}$ radians in θ and then performing a full 2π rotation in ϕ.

Figure 2.8: The probability density of the doughnut shaped state which is stabilized by the potential with positive values of a, b ~ 0.

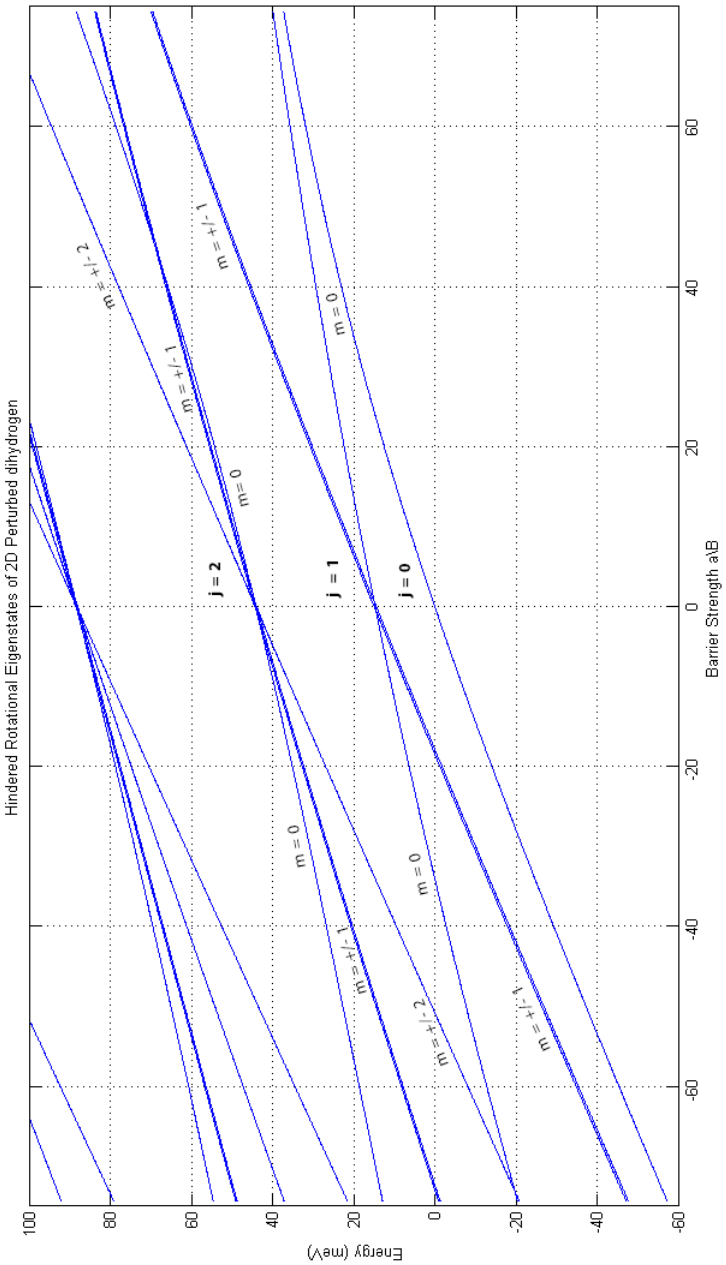

Figure 2.9: The rotational energy spectrum for hydrogen interacting with an anisotropic potential. When a = b = 0, the energy levels are characteristic of the free rotator.

When b $\sim$0, and a < 0, then the potential is most attractive when the molecule lies parallel to the surface. These states are represented by the planar, ring doughnut shaped wavefunctions $|11\rangle$. The relative energies of the m states fall as the potential deepens, but remain degenerate. The molecular axis is unhindered in ϕ if b=0, but becomes more hindered as b increases. As a becomes more negative (attractive), the potential well securing the molecule to the surface deepens, and the dumbbell shaped state $|10\rangle$ becomes more energetic. In the limit of very large negative values of a, the polar angle θ is now $\frac{\pi}{2}$ and the energy of the first rotational transiton approaches $B_{H_2} = 7.35\ meV$. The energies in the limit of very large negative values of a are the energies of a rotator confined to a plane with the axis of rotation being normal to the surface. When b $\sim$0, and a > 0, the potential is most attractive (minimized) when the molecular axis is normal to the surface. The state stabilized by this potential is now the $|10\rangle$ state as shown in figure 2.9, as the energy of this state decreases as a increases. In the limit of very large values of a, the potential strongly constrains the molecular axis to the axis of rotation normal to the surface. The energies of the $|00\rangle$ and $|10\rangle$ states begin to converge and the energy for this transition becomes negligible. In the case of D_2 (included for completeness Fig 2.10), much is the same except that the derivative of the energy with respect to barrier strength is much greater than that of H_2 which is due to $B_{H_2} = 2B_{D_2}$

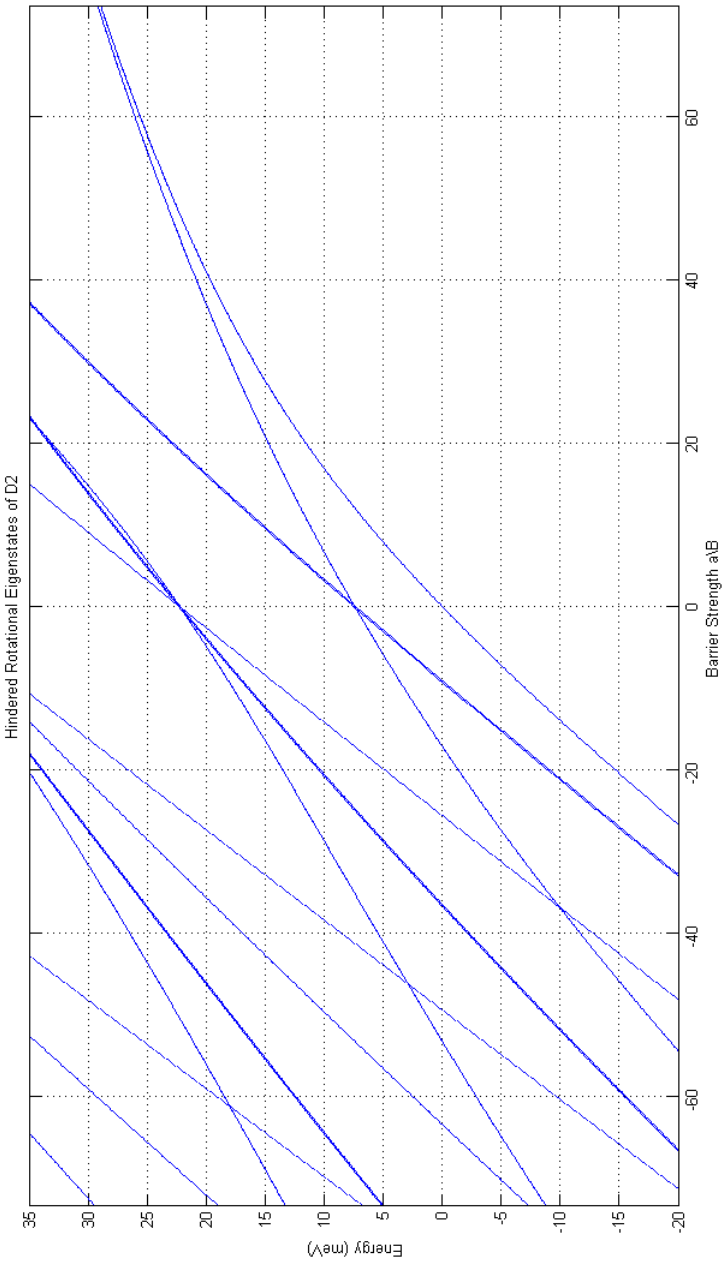

Figure 2.10: The rotational energy spectrum for dideuterium interacting with an anisotropic potential. When a = b = 0, the energy levels are characteristic of the free rotator.

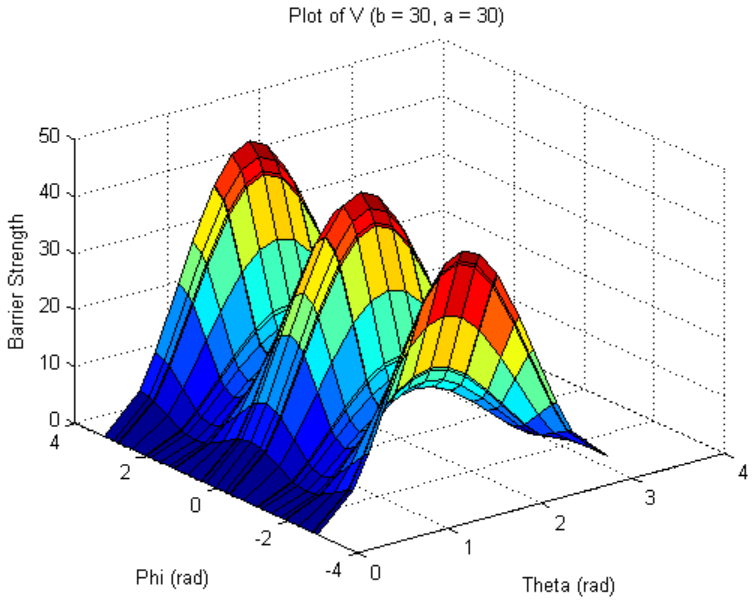

(a)

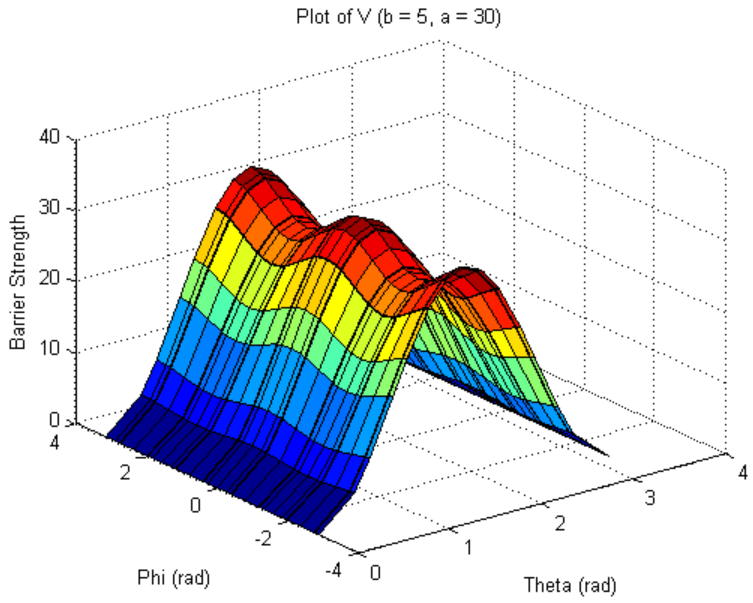

(b)

Figure 2.11: (a) An example of a strong field in b, which strongly hinders the rotation about angle phi greatly raising the degeneracy of the j = 1 state. (b) An example of a weak field in b, which weakly hinders the rotation about angle phi, minimally raising the degeneracy of the j = 1 state.

Recall that b is the parameter which determines the hindering strength of the potential relative to the azimuthal angle ϕ. As this parameter increases, the degeneracies in the j = 1 states are lifted. Figure 2.11 illustrates how the potential behaves as a function of this change. In 2.11b, b = 5 which represents a weak field in b. The rotation about the angle ϕ is not significantly hindered as the wells which are beginning to form in contrast to figure 2.7a allow for some movement over the center hump. In 2.11a, b = 30, which represents a strong field in b. The wells have become much deeper now and the energy required to rotate across the barrier is significant. Since the moment of inertia of deuterium is twice that of hydrogen, it would require twice the rotational barrier strength to achieve the same splitting in the j = 1 dihydrogen states. By now having the computational framework established for calculating the energy spectrum of these simple systems, the driving force now is to extend the usefulness to more complicated systems.

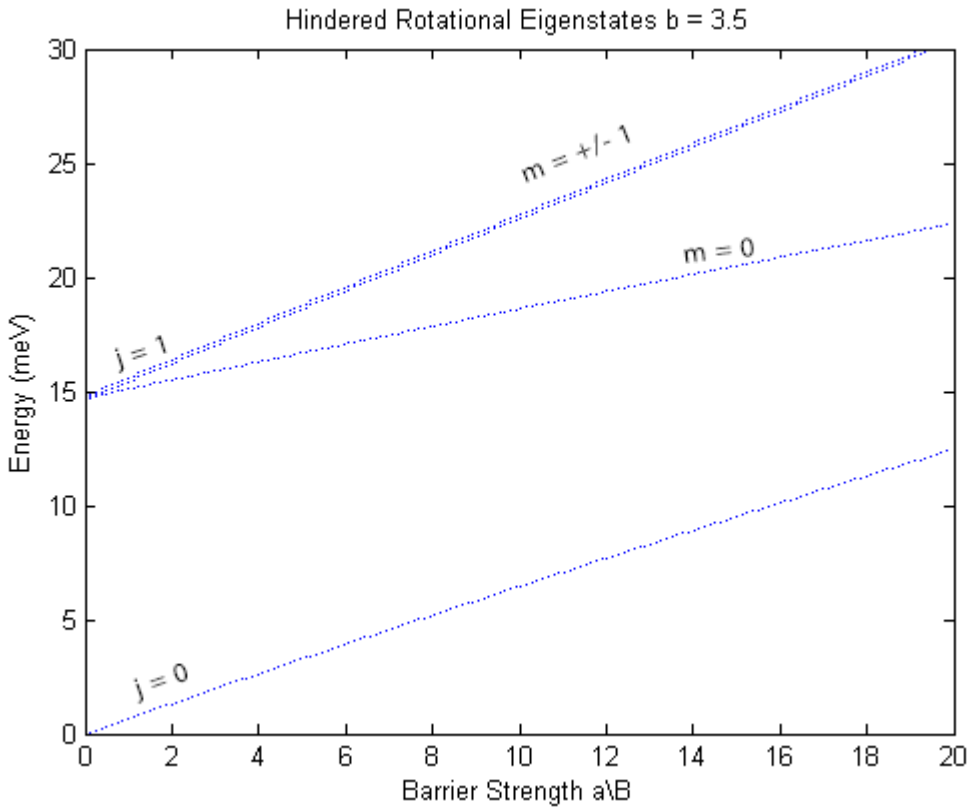

Figure 2.12: A zoomed in view of the splitting of the j = 1 states for dihydrogen.

Bibliography

Becke, A. D. (1988). A multicenter numerical-integration scheme for polyatomic-molecules. *Journal of Chemical Physics*, 88(4):2547–2553. M1104 Times Cited:1397 Cited References Count:41. 26

Cotton, F. A. (1990). *Chemical applications of group theory*. Wiley, New York, 3rd edition. 89016434 (Frank Albert), F. Albert Cotton. ill. ; 25 cm. Tables in pocket. "A Wiley-Interscience publication." Bibliography: p. 452-455. 17

Freitag, A. and Larese, J. Z. (2000). Layer growth of methane on MgO: An adsorption isotherm study. *Physical Review B*, 62(12):8360–8365. 359CF Times Cited:21 Cited References Count:19. 5, 9

Henrich, V. E. and Cox, P. A. (1994). *The surface science of metal oxides*. Cambridge University Press, Cambridge ; New York. 93018566 Victor E. Henrich and P.A. Cox. ill. ; 26 cm. Includes bibliographical references (p. 431-458) and indexes. 5

Joshi, R. K., Hu, Q., Alvi, F., Joshi, N., and Kumar, A. (2009). Au decorated zinc oxide nanowires for CO sensing. *The Journal of Physical Chemistry C*, 113(36):16199–16202. 10

Larese, J. and Kunnmann, W. (2001). Method for the generation of variable density metal vapors which bypasses the liquidus phase. B1(09/271890):7. 3, 6

Larese, J. Z., Arnold, T., Barbour, A., and Frazier, L. R. (2009). Neutron investigations of rotational motions in monolayer and multilayer films at the interface of MgOand graphite surfaces. *Langmuir*, 25(7):4078–4083. 427RY Times Cited:8 Cited References Count:39. xi, 17, 18, 19

Lebedev, V. I. (1976). One type of quadrature formulas of algebraic multiple precision for sphere. *Doklady Akademii Nauk Sssr*, 231(1):32–34. Cs335 Times Cited:3 Cited References Count:3. 26

Li, H., Huang, Y., Zhang, Y., Qi, J., Yan, X., Zhang, Q., and Wang, J. (2009). Self-catalytic synthesis, structures, and properties of high-quality tetrapod-shaped ZnO nanostructures. *Crystal Growth & Design*, 9(4):1863–1868. 11

MacRury, T. B. (1969). *Hindered Rotation of Diatomic Molecules in the Adsorbed Phase*. PhD thesis. 29

Macrury, T. B. and Sams, J. R. (1970). Hindered rotation of adsorbed diatomic molecules 1. eigenvalues and eigenstates of hindered rotator. *Molecular Physics*, 19(3):337–352. 30

Miura, Y., Kasai, H., Dio, W., and Okiji, A. (1999). Vibrational and rotational coupling effects in the direct scattering of H2 from Cu(111). *Surface Science*, 438(13):254 – 260. xi, 30

Pauling, L. (1930). The rotational motion of molecules in crystals. *Physical Review*, 36(3):430–443. 1

Sandler, Y. L. (1954). The adsorption and ortho-para conversion of hydrogen on diamagnetic solids 2. the relative adsorbabilities of orthohydrogen and parahydrogen. *Journal of Physical Chemistry*, 58(1):58–61. Um479 Times Cited:71 Cited References Count:6. 16

Scamehorn, C. A., Harrison, N. M., and McCarthy, M. I. (1994). Water chemistry on surface defect sites: Chemidissociation versus physisorption on MgO(001). *The Journal of Chemical Physics*, 101(2):1547. 1

Van de Walle, C. G. (2000). Hydrogen as a cause of doping in zinc oxide. *PHYSICAL REVIEW LETTERS*, 85(5):1012–1015. 339BD Times Cited:1005 Cited References Count:15. 9

Wang, X. G. and Carrington, T. (2003). Using lebedev grids, sine spherical harmonics, and monomer contracted basis functions to calculate bending energy levels of HF trimer. *Journal of Theoretical & Computational Chemistry*, 2(4):599–608. 812VQ Times Cited:10 Cited References Count:27. 26

Wang, Z. L. (2004). Nanostructures of zinc oxide. *Materials Today*, 7(6):26 – 33. 10

White, D. and Lassettre, E. N. (1960). Theory of ortho-para hydrogen separation by adsorption at low temperatures, isotope separation. *Journal of Chemical Physics*, 32(1):72–84. Wb887 Times Cited:107 Cited References Count:12. 33

Yu, Y., Guo, Q., Liu, S., Wang, E., and Mller, P. (2003). Partial dissociation of water on a MgO(100) film. *Physical Review B*, 68(11). 3

Appendix

Appendix A

MATLAB Code

A.1 Matrix Mechanics Method

```
%%  This program solves the rotational eigenvalue problem for hydrogen in a 2-D potential
% using a basis of l spherical harmonics

%% // prereqs
% // Value of l to use
degree=7;
B = 59.3; % Rotational constant for dihydrogen in wavenumber
b = 0.17;
c = 0.1239842; % conversion factor from wavenumber to meV for JZL
hbar = 1.05457173E-34;
boltz = 1.3806488E-23;
T = 20.4 + 273.15;
%% // build the Lebedev Sphere using 230 pts - theta is the alt., phi is the az.
leb = getLebedevSphere(230);
phi = atan2(leb.y,leb.x);
theta = acos(leb.z);
phi2 = sort(phi);
theta2 = sort(theta);
[U, V] = meshgrid(theta2,phi2);
```

```
%% // Calculate the total number of basis functions

fns = 0;

for kk = 0:degree
    numfun = 2*kk + 1;
    fns = fns + numfun;
    numfun = 0;
end

%% // Allocate the matrices
v = zeros(size(phi,1),1);
H = zeros(fns,fns);
J = [0 1 1 1 2 2 2 2 2 3 3 3 3 3 3 3 4 4 4 4 4 4 4 4 4 5 5 5 5 5 5
5 5 5 5 5 6 6 6 6 6 6 6 6 6 6 6 6 6 6 7 7 7 7 7 7 7 7 7 7 7 7 7 7];

%% // construct the Spherical Harmonics basis over theta and phi

k =(degree + 1)*(degree + 1);  %% k is the # of coefficients
Y = zeros(length(leb.x),k);
for l = 0:degree
    Pm = legendre(l,leb.z); % legendre part
    Pm = Pm';
    lconstant = sqrt((2*l + 1)/(4*pi));
    % calculate where to put the vector
    center = (l+1)*(l+1) - l;
    % calculate the Yl0
    Y(:,center) = lconstant.*Pm(:,1);
    % calculate the other Ylm of the set (if any)
    for m=1:l
        precoeff = lconstant * sqrt(factorial(l - m)/factorial(l + m));
       if mod(m,2) == 1
          Y(:, center + m) = precoeff.*Pm(:,m+1).*exp(1i*m*phi);
          Y(:, center - m) = -precoeff.*Pm(:,m+1).*exp(-1i*m*phi);
```

```
        else
           Y(:, center + m) = precoeff.*Pm(:,m+1).*exp(1i*m*phi);
           Y(:, center - m) = precoeff.*Pm(:,m+1).*exp(-1i*m*phi);
       end
    end
end

%% // Generate the potential matrix

for a = -600:1:600

for m = 1:size(phi,1)
      v(m,1) = a*c*(sin(theta(m)).^2) + (0.5*b*c).*
                     (cos(2*phi(m)).*(sin(theta(m))).^2);
      %v(m,1) = a*cos(theta(m)).^2;
end

% make an array that relates the index n to QM J.
for m = 1:fns
    for n = 1:fns
        pre_v = sum(conj(Y(:,m)).*v.*Y(:,n).*leb.w);
        if m == n
        H(n,n) = B*c*J(n)*(J(n)+1) + sum(conj(Y(:,n)).*v.*Y(:,n).*leb.w);
        else
            H(m,n) = pre_v;
        end
    end
end

%% // diagonalize the matrix, generating energies and a new basis
[new_basis,eigenvalues] = eig(H);
sorted = sort(diag(real(eigenvalues)));
% figure(1)
% plot(a*c,sorted(1));
```

```
% plot(a*c,sorted(2));
% plot(a*c,sorted(3));
% plot(a*c,sorted(4));
% plot(a*c,sorted(5));
% plot(a*c,sorted(6));
% plot(a*c,sorted(7));
% plot(a*c,sorted(8));
% plot(a*c,sorted(9));
% refreshdata
% drawnow
% hold on
%% Calculate the separation factor and plot a vs. s
conv = 1.602177E-22; % conv Joule to meV
S = (2/3)*exp((2*hbar^2)/(8*pi^2*boltz*T)) -
       conv*(sorted(4) - sorted(1))/(boltz*T) + 1/3 -
       conv*(sorted(3)-sorted(2))/(boltz*T);
plot(a*c,S)
hold on
% %% Plot the potential
% for i = 1:length(theta)
%     for j = 1:length(phi)
%     potential(i,j) =  a*(sin(theta2(j)).^2) + (0.5*3).*
                                (cos(2*phi2(i)).*(sin(theta2(j))).^2);
%     end
% end
% figure(3)
% surf(U,V,potential);
%  axis([0 4 -4 4 -600 600])

end  %//end iteration over various potential heights
```

A.2 Code for Clebsch-Gordan Routine

```
%Program which will attempt to solve the schrodinger equation for the
%out of plane hindered rotor using Clebsch-Gordan Coefficients
%Written by George Rouvelas \\ February, 2013 UTK \\
%This program relies on the clebsch-gordan coefficient subroutine

clear
clc

%Initialize the loop which diagonalizes the Hamiltonian for each value of
%the barrier height.  Later in this loop a loop over the allowed m quantum
%numbers will be added
for m=1:1:3
for lambda = 0:5:2500

%Preallocate matrices with zeros and initialize the dummy variables
[V]      =   zeros(10,10);
[E]      =   zeros(10,10);
[Eeven]  =   zeros(5,5);
[Eodd]   =   zeros(5,5);
[Vodd]   =   zeros(5,5);
[Veven]  =   zeros(5,5);
B        =   60.853; %This is the rotational constant for H2 in wavenumber
%m        =   0; %m cannot start at 0 because it's in for loop so real value is m-1
k        =   0;
z        =   0;
lprime   =   0;
%Using the Wigner 3j coefficients subroutine, the potential matrix V is
%built from a basis of 100 spherical harmonics (0.le.lambda.le.9) with the
%conditional statements enforcing the selection rules

for l=1:1:10
```

```
    E(l,l)=B*((l-1)*((l-1)+1));

    for lprime=1:1:10

        if m > lprime || m > l
        V(l,lprime) = 0;
        continue
        end
        if abs((l-1)-(lprime-1)) == 2 && (-1)^(l-1) == (-1)^(lprime-1)
        V(l,lprime)=((2/3)*((2*(l-1)+1)/(2*(lprime-1)+1))^(0.5))*
         clebschgordan( l-1, m-1, 2, 0, lprime-1, m-1)*
         clebschgordan( l-1, 0, 2, 0, lprime-1, 0);
        end
        if (l-1) == (lprime-1) && (-1)^(l-1) == (-1)^(lprime-1)
        V(l,lprime) = ((2/3)*((2*(l-1)+1)/(2*(lprime-1)+1))^(0.5))*
        clebschgordan( l-1, m-1, 2, 0, lprime-1, m-1)*
        clebschgordan( l-1, 0, 2, 0, lprime-1, 0)
       + ((1/3)*((2*(l-1)+1)/(2*(lprime-1)+1))^(0.5))*
        clebschgordan( l-1, m-1, 0, 0, lprime-1, m-1)*
        clebschgordan( l-1, 0, 0, 0, lprime-1,0);
        end
    end
end

%now I split up the Perturbation Matrix and Free Rotor Matrix by parity with p=(-1)^^l
%p=-1
for i = 1:2:9
    for j = 1:2:9
        Vodd(1+z,1+k) = V(i,j);
        Eodd(1+z,1+k) = E(i,j);
        k=k+1;
    end
    z=z+1;
    k=0;
```

```
end

%p=+1
%reuse k and z here
z = 0;
k = 0;

for i = 2:2:10
    for j = 2:2:10
        Veven(1+z,1+k) = V(i,j);
        Eeven(1+z,1+k) = E(i,j);
        k = k+1;
    end
    z = z+1;
    k = 0;
end

%Build up the total Hamiltonian
[Hodd] = Eodd + lambda.*Vodd;
[Heven] = Eeven + lambda.*Veven;

%Diagonalize the Hamiltionian
[oddbasis,oddenergies] = eig(Hodd);
[evenbasis,evenenergies] = eig(Heven);
low_odd_e=oddenergies(1,1);
low_even_e=evenenergies(1,1);



for y=1:1:5

        if oddenergies(y,y)< low_odd_e && oddenergies(y,y) ~=0
            low_odd_e=oddenergies(y,y);
        end
```

```
end

y=0;


for y=1:1:5

        if evenenergies(y,y) < low_even_e && evenenergies(y,y) ~= 0
            low_even_e=evenenergies(y,y);
        end

end

if m == 3
    plot(lambda,evenenergies(4,4));
else plot(lambda,low_even_e);
end
plot(lambda,low_odd_e);
hold on


end
end
```

A.3 Clebsch-Gordan subroutine

```
% Thanks to Oliver Johnson for assistance with this subroutine
function C = clebschgordan(j1,m1,j2,m2,j,m)

assert(isscalar(j1) && isscalar(m1) && isscalar(j2) && isscalar(m2)
          && isscalar(j) && isscalar(m),'All inputs must be scalars.')

%satisfy conditions
if j1 < 0 || j2 < 0 || j < 0 || ...
        mod(2*j1,1) ~= 0 || mod(2*j2,1) ~= 0 || mod(2*j,1) ~= 0 || ...
        mod(2*m1,1) ~= 0 || mod(2*m2,1) ~= 0 || mod(2*m,1) ~= 0 || ...
        abs(m1) > j1 || abs(m2) > j2 || abs(m) > j || ...
        j1+m1 < 0 || j2+m2 < 0 || j+m < 0 || j1+j2+j < 0 ||...
        mod(j1+m1,1) ~= 0 || mod(j2+m2,1) ~= 0 || mod(j+m,1) ~= 0 || ...
        mod(j1+j2+j,1) ~= 0

    error(sprintf('Clebsch-Gordan coefficient only defined if:
 \n 1. j1, j2, j are integer or half-integer non-negative numbers.
 \n 2. m1, m2, m are integer or half-integer numbers. \n 3. abs(m1)<=j1,
 abs(m2)<=j2, abs(m)<=j \n 4. j1+m1, j2+m2, j+m,
 j1+j2+j are integer non-negative numbers.')) %#ok<SPERR>

elseif m1+m2-m ~= 0 || j < abs(j1-j2) || j > j1+j2

    C = 0;
    return

end

%compute valid k values for summation
k = max([0,j2-j-m1,j1-j+m2]):min([j1+j2-j,j1-m1,j2+m2]);

%check stability
if j+j1-j2 > 21 || j+j2-j1 > 21 || j1+j2-j > 21 || j1+j2+j+1 > 21 || ...
```

```
        j+m > 21 || j-m > 21 || j1+m1 > 21 || j1-m1 > 21 || ...
        j2+m2 > 21 || j2-m2 > 21 || any(k > 21) || ...
        any(j1+j2-j-k > 21) || any(j1-m1-k > 21) || ...
        any(j2+m2-k > 21) || any(j-j2+m1+k > 21) || any(j-j1-m2+k > 21)

    warning('The argument to one or more of the factorials used in the computation of the
 requested Clebsch-Gordan coefficient is greater than 21,
 this can result in inaccuracies (see Matlab documentation
for the FACTORIAL function).') %#ok<WNTAG>

end

%now compute the coefficients
C = sqrt((2*j+1)*factorial(j+j1-j2)*factorial(j+j2-j1)*
      factorial(j1+j2-j)/factorial(j1+j2+j+1))*...
    sqrt(factorial(j+m)*factorial(j-m)*factorial(j1+m1)*
    factorial(j1-m1)*factorial(j2+m2)*factorial(j2-m2))*...
    sum(((-1).^k)./(factorial(k).*factorial(j1+j2-j-k).*
     factorial(j1-m1-k).*factorial(j2+m2-k).*factorial(j-j2+m1+k).*factorial(j-j1-m2+k)));
```

Vita

George Rouvelas was born in Manchester, TN on January 22, 1987 to Tony and Lisa Rouvelas and is the proud big brother of Alexis Rouvelas. After moving to several different locations thoughout Tennessee and Georgia, his family settled in Madisonville, TN where he spent most of his childhood as his parents managed a successful restaurant business. He attended Sequoyah High School in 2001 and graduated in 2005 with a science and engineering concentration. After graduating high school, he started his Bachelor of Science degree at the University of Tennessee, Knoxville with a major in Chemical Engineering. After interning in the field, he decided that a change in major to Chemistry was needed. He then began undergraduate research with Dr. Robert J. Hinde writing code to calculate some chemical properties of the hydrogen molecule. He then completed his Honors Bachelor of Science degree in 2009 and pursued a Ph.D at Vanderbilt University. Following a change of heart, he decided to move back to Knoxville to pursue a Master of Science degree with Professor John Z. Larese in the spring of 2011.